Polarization Accuracy Verification of the Chromospheric LAyer SpectroPolarimeter

Donguk Song[1,2] · Ryohko Ishikawa[2] · Ryouhei Kano[2] · David E. McKenzie[3] · Javier Trujillo Bueno[4,5,6] · Frédéric Auchère[7] · Laurel A. Rachmeler[8] · Takenori J. Okamoto[2] · Masaki Yoshida[2,9] · Ken Kobayashi[3] · Christian Bethge[10] · Hirohisa Hara[2] · Kazuya Shinoda[2] · Toshifumi Shimizu[11] · Yoshinori Suematsu[2] · Bart De Pontieu[12,13,14] · Amy Winebarger[3] · Noriyuki Narukage[2] · Masahito Kubo[2] · Taro Sakao[11] · Andrés Asensio Ramos[4,5] · Luca Belluzzi[15,16,17] · Jiří Štěpán[18] · Mats Carlsson[13,14] · Tanausú del Pino Alemán[4,5] · Ernest Alsina Ballester[15] · Genevieve D. Vigil[3,19] · Jorrit Leenaarts[20]

✉ D. Song
donguksong@kasi.re.kr

[1] Korea Astronomy and Space Science Institute, 776 Daedeok-daero, Yuseong-gu, Daejeon 34055, Republic of Korea

[2] National Astronomical Observatory of Japan, 2-21-1 Osawa, Mitaka, Tokyo 181-8588, Japan

[3] NASA Marshall Space Flight Center, Huntsville, AL 35812, USA

[4] Instituto de Astrofísica de Canarias, E-38205 La Laguna, Tenerife, Spain

[5] Departamento de Astrofísica, Universidad de La Laguna, E-38206 La Laguna, Tenerife, Spain

[6] Consejo Superior de Investigaciones Científicas, Spain

[7] Institut d'Astrophysique Spatiale, 91405 Orsay Cedex, France

[8] National Oceanic and Atmospheric Administration, National Centers for Environmental Information, Boulder, CO 80305, USA

[9] Department of Astronomical Science, School of Physical Sciences, SOKENDAI (The Graduate University for Advanced Studies), Mitaka, Tokyo 181-8588, Japan

Abstract We have developed an advanced UV spectropolarimeter called Chromospheric LAyer SpectroPolarimeter (CLASP2), aimed at achieving very high accuracy measurements (<0.1% at 3σ) of the linear (Q/I and U/I) and circular (V/I) polarizations of the Mg II h and k lines (280 nm). CLASP2 was launched on board a NASA sounding rocket on April 11, 2019. It successfully detected the full Stokes vector in an active region plage and in the quiet Sun near the limb across the Mg II h and k lines for the first time. To verify the polarization characteristics of CLASP2, the response matrix is estimated by combining the results obtained from the pre-flight calibration on the ground, with the results of the in-flight calibration acquired at the solar disk center. We find that the response matrix of CLASP2 in the Mg II h and k lines is notably close to an ideal response matrix, i.e., the scale factor and the crosstalk terms are close to 1 and 0, respectively. Moreover, the uncertainty of each Stokes parameter estimated by the repeatability of the measurements is verified to be within the required tolerance. Based on our investigation, we conclude that CLASP2 achieves 0.1%polarization accuracy at a 3σ level.

Keywords: Magnetic fields, Chromosphere; Instrumental Effects; Spectropolarimetry, Ultraviolet

[10] Cooperative Institute for Research in Environmental Sciences, University of Colorado at Boulder, Boulder, CO 80305, USA

[11] Institute of Space and Astro-nautical Science, Japan Aerospace Exploration Agency, Sagamihara, Kanagawa 252-5210, Japan

[12] Lockheed Martin Solar & Astro-physics Laboratory, Palo Alto, CA 94304, USA

[13] Rosseland Centre for Solar Physics, University of Oslo, NO-0315 Oslo, Norway

[14] Institute of Theoretical Astrophysics, University of Oslo, NO-0315 Oslo, Norway

[15] Istituto Ricerche Solari (IRSOL), Università della Svizzera italiana (USI), CH-6605 Locarno Monti, Switzerland

[16] Leibniz-Institut für Sonnenphysik (KIS), Schöneckstr. 6, D-79104, Freiburg, Germany

[17] Euler Institute, Università della Svizzera italiana (USI), CH-6900 Lugano, Switzerland

[18] Astronomical Institute, Academy of Sciences of the Czech Republic, 25165 Ondrejov, Czech Republic

[19] Universities Space Research Association, Huntsville, AL 35805, USA

[20] Institute for Solar Physics, Department of Astronomy, Stockholm University, AlbaNova University Centre, SE-106 91, Stockholm, Sweden

1. Introduction

The solar chromosphere is an inhomogeneous region that is full of fine-scale structures undergoing a variety of dynamics and heating phenomena. Over the last 10 years, advanced multi-wavelength observations have demonstrated that such chromospheric structures are crucial to the supply and balance of mass and energy in the outer solar atmosphere.

The Mg II h and k resonance lines (around 280 nm) are some of the strongest chromospheric lines and have been widely used to explore the upper solar chromosphere. In particular, the unprecedented high-resolution spectroscopic observations provided by the Interface Region Imaging Spectrograph (IRIS; De Pontieu et al., 2014b) have revolutionized our understanding of the critical role of this highly dynamic interface region between the photosphere and the corona, e.g., the mechanism behind excitation and propagation of magnetohydrodynamic waves (Tian et al., 2014; Song et al., 2017b), plasma ejections and heating phenomena (De Pontieu et al., 2014a), and transport and dissipation of energy (Okamoto et al., 2015; De Pontieu et al., 2021). Despite these recent advances, our lack of empirical knowledge regarding the direction and strength of magnetic fields in the chromosphere is a major impediment to a better understanding of the solar atmosphere.

The direct measurement of magnetic fields in the solar chromosphere is one of the major remaining challenges in solar physics. In the past decade, several theoretical studies have predicted that these magnetic fields can produce measurable modifications in the polarization Q/I profiles across the Mg II h and k lines (Belluzzi and Trujillo Bueno, 2012; del Pino Alemán, Casini, and Manso Sainz, 2016; del Pino Alemán et al., 2020; Alsina Ballester, Belluzzi, and Trujillo Bueno, 2016). Belluzzi and Trujillo Bueno (2012) theoretically predicted a pattern of the near-limb scattering polarization profile in the range of 279.0−280.7 nm based on an advanced radiative transfer calculation using a semi-empirical model of the quiet-Sun atmosphere. Their calculated Stokes Q/I profile shows a complex pattern, in which the core of the Mg II k line contains a positive line-center signal with an amplitude of 1.5%, surrounded by two negative peaks at the blue and red near-line wings. Additionally, the far blue and red wings show positive Q/I signals, and the line wing between Mg II h and k presents negative polarization. We note that positive and negative signs of Q/I are defined as parallel and perpendicular to the solar limb, respectively. Belluzzi and Trujillo Bueno (2012) demonstrated that such a complex Q/I pattern results from the joint action of the partial frequency redistribution and quantum interference between the upper J-levels of the two lines (J-state interference). In addition, they showed that there is no scattering polarization at the center of the Mg II h line, and that its Q/I profile is antisymmetric.

Alsina Ballester, Belluzzi, and Trujillo Bueno (2016); del Pino Alemán, Casini, and Manso Sainz (2016); and del Pino Alemán et al. (2020) showed that the amplitudes of the Stokes Q/I and U/I profiles at the Mg II k line center are modified by more than 0.1% due to the Hanle effect, if the magnetic field strength is $\geq$ 10 G. In addition, the amplitudes of wings of the Mg II h and k lines may change more than 0.1% due to magneto-optical effects. On the other hand,

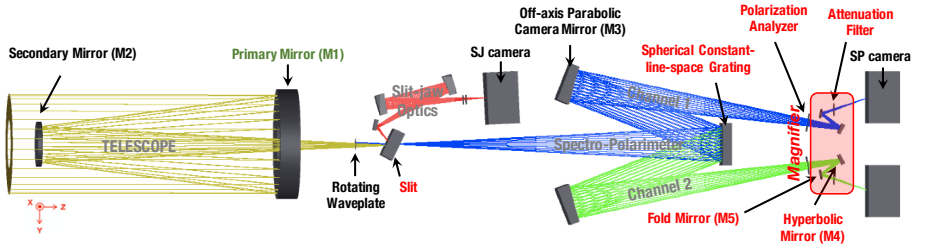

Figure 1. Optical design of CLASP2. The coordinate system of the mechanical axis of CLASP2 is shown with *red arrows*. The X-axis corresponds to the slit direction. The *black text* indicates the optical elements in common with CLASP1, whereas the *red text* indicates the new optics and structures in CLASP2. The *green text* indicates the re-coated mirror of CLASP2.

circular polarization signals (V/I) are introduced at both the Mg II h and k lines by the Zeeman effect. Previous theoretical studies have showed that a 10 G longitudinal magnetic field produces a 0.1% circular polarization signal. These theoretical results clearly indicate that a polarization accuracy greater than 0.1% with a spectral resolution of 0.01 nm and a spatial resolution of the order of 10 arcsec is required to investigate the magnetic fields in the quiet regions of the upper chromosphere.

An advanced UV spectropolarimeter, named Chromospheric LAyer SpectroPolarimeter (hereafter, CLASP2; Narukage et al., 2016), was developed to investigate the magnetic fields of the upper solar chromosphere using the spectropolarimetry across the Mg II h and k lines in the near-UV spectral window of 279.985 ± 0.45 nm at 0.1% polarization accuracy. On April 11, 2019, CLASP2 was launched at White Sands Missile Range. It successfully detected full Stokes profiles of an active region plage (Ishikawa et al., 2021) and of a quiet region near the limb (Rachmeler et al., 2022; submitted). In this study, the polarization characteristics of CLASP2 are verified by determining its response matrix.

2. The CLASP2 Instrument

CLASP2 follows the successful design of the Chromospheric Lyman-Alpha SpectroPolarimeter (hereafter CLASP1; Kano et al., 2012; Narukage et al., 2015), which was the first to measure the linear polarization in the hydrogen Lyα line (121.57 nm; Kano et al., 2017) and the Si III line (120.65 nm; Ishikawa et al., 2017). Figure 1 shows the optical design of CLASP2, which has been modified from CLASP1. CLASP2 is designed as an optically symmetric structure consisting of a classical Cassegrain telescope with an aperture of ϕ270 mm, slit-jaw optics (SJ; Kubo et al., 2016), and a dual-channel spectropolarimeter. We reused many individual components (labeled with black text in Figure 1) and the main structure of CLASP1. Minimal modifications (labeled with green and red text in Figure 1) were made to optimize for the new spectral window of the Mg II h and k lines required for CLASP2. The major design change from CLASP1 is a new magnifying optical system (red box in Figure 1), which is newly installed in front

of the two spectropolarimeter cameras. This system doubles the focal length to achieve the same spectral resolution as CLASP1 (0.01 nm) while maintaining the same dispersion angle for the longer wavelength of CLASP2, and thus allowing to reuse the main structure and M3 mirror. Meanwhile, the CLASP2/SJ optics remains unchanged from CLASP1 and performs the Lyα imaging observations around the slit. The primary mirror was recoated as a dual-band pass cold mirror (green text in Figure 1) to achieve high reflectivity not only in the new spectral window of the Mg II h and k lines (280 nm) for the spectropolarimeter, but also in the Lyα line for the SJ system. A detailed explanation of the new design is given in Tsuzuki et al. (2020). Moreover, the integration and the optical alignment of CLASP2 are explained in Song et al. (2018) and Yoshida et al. (2018).

2.1. The Polarimeter System of CLASP2

The polarimeter of CLASP2 is composed of a Polarization Modulation Unit (PMU; Shimizu et al., 2014; Ishikawa et al., 2015) and two transmissive polarization analyzers. The PMU continuously executes one homogeneous rotation every 3.2 **s**, and contains a compound zero-order MgF_2 waveplate (Ishikawa et al., 2013). We measured the birefringence of the MgF_2 around the 280 nm wavelength at the UltraViolet Synchrotron Orbital Radiation (UVSOR) facility. The phase retardations of the CLASP1 waveplate are evaluated to be $234.5°\pm1°$ at the Mg II k line (279.64 nm) and $233.6°\pm1°$ at the Mg II h line (280.35 nm), which results in comparable modulation efficiencies for both the linear and circular polarizations. Thus, the CLASP1 waveplate was reused in CLASP2. A phase retardation of 234° is used for CLASP2 demodulation.

The ±1st order beams, which are dispersed by a newly fabricated grating, pass through the transmissive polarization analyzers that are installed in front of the magnifying optical system for each channel (Figure 1). The polarization analyzers are "wire grid" linear polarizers (Berger et al., 2012) with their principal axes placed in the Y-direction of the CLASP2 mechanical axis (perpendicular to the slit) for channel 1 and in the X-direction for channel 2 (parallel to the slit). This set-up allows the measurement of two orthogonal polarizations simultaneously.

3. Polarization Measurement

3.1. Definition of CLASP2 Polarization Coordinates

Figure 2 shows the polarization coordinate system as viewed from the entrance aperture of CLASP2. The $+Q$ direction is defined parallel to the slit direction, which corresponds to the X-axis of the CLASP2 mechanical axis, and each direction of the linear Stokes vectors ($+U$, $-Q$, and $-U$) is defined clockwise at 45° intervals, respectively. This definition is identical to that in Giono et al. (2016). Finally, the $+V$ direction is defined as the direction of the electric vector rotating clockwise as viewed from the entrance aperture of the instrument, and its opposite direction is defined $-V$.

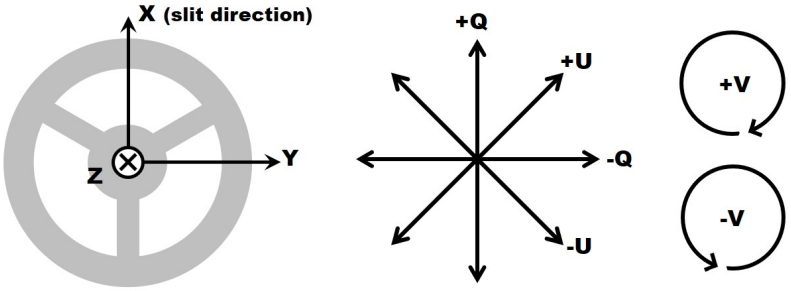

Figure 2. Polarization coordinates as viewed from the entrance aperture of CLASP2.

3.2. Polarization Modulation

The interaction of light with optical elements in CLASP2 can result in the linear transformation of the incoming Stokes vectors ($\boldsymbol{S}$). The ruling direction of the grating and the slit are parallel to one of the principal axes of the polarization analyzers and the M3 mirrors are tilted around the same axis. Thus, such an interaction can be represented by the polarizing elements of CLASP2, i.e., a polarization analyzer with the orientation α and the MgF_2 waveplate with the fast-axis angle ϕ and phase retardation δ. This polarization response of the instrument can be represented by **a** 4×4 Mueller matrix, $\mathbf{M}_{(\alpha,\delta,\phi)}$=$\mathbf{M}_P(\alpha)\mathbf{M}_W(\delta,\phi)$, and the demodulated Stokes vector $\boldsymbol{S}'$ can be expressed as $\boldsymbol{S}' = \mathbf{M}_{(\alpha,\delta,\phi)}\boldsymbol{S}$;

$$\boldsymbol{S}' = \mathbf{M}_{(\alpha,\delta,\phi)}\boldsymbol{S} = \begin{pmatrix} I' \\ Q' \\ U' \\ V' \end{pmatrix} = \begin{pmatrix} \boldsymbol{m}_{11} & \boldsymbol{m}_{12} & \boldsymbol{m}_{13} & \boldsymbol{m}_{14} \\ \boldsymbol{m}_{21} & \boldsymbol{m}_{22} & \boldsymbol{m}_{23} & \boldsymbol{m}_{24} \\ \boldsymbol{m}_{31} & \boldsymbol{m}_{32} & \boldsymbol{m}_{33} & \boldsymbol{m}_{34} \\ \boldsymbol{m}_{41} & \boldsymbol{m}_{42} & \boldsymbol{m}_{43} & \boldsymbol{m}_{44} \end{pmatrix} \begin{pmatrix} I \\ Q \\ U \\ V \end{pmatrix} = \begin{pmatrix} \boldsymbol{m}_{11}\mathrm{I}+\boldsymbol{m}_{12}\mathrm{Q}+\boldsymbol{m}_{13}\mathrm{U}+\boldsymbol{m}_{14}\mathrm{V} \\ \boldsymbol{m}_{21}\mathrm{I}+\boldsymbol{m}_{22}\mathrm{Q}+\boldsymbol{m}_{23}\mathrm{U}+\boldsymbol{m}_{24}\mathrm{V} \\ \boldsymbol{m}_{31}\mathrm{I}+\boldsymbol{m}_{32}\mathrm{Q}+\boldsymbol{m}_{33}\mathrm{U}+\boldsymbol{m}_{34}\mathrm{V} \\ \boldsymbol{m}_{41}\mathrm{I}+\boldsymbol{m}_{42}\mathrm{Q}+\boldsymbol{m}_{43}\mathrm{U}+\boldsymbol{m}_{44}\mathrm{V} \end{pmatrix}. \quad (1)$$

As shown in Equation 1, the expression of the matrix is complicated, but only the intensity, which is an element of the first row of the matrix ($I' = \boldsymbol{m}_{11}I + \boldsymbol{m}_{12}Q + \boldsymbol{m}_{13}U + \boldsymbol{m}_{14}V$), is actually recorded in the spectropolarimeter cameras. Here, $\boldsymbol{m}_{11} = \frac{1}{2}$, $\boldsymbol{m}_{12} = \frac{1}{2}[\cos 2\alpha(\cos 2\phi + \sin^2 2\phi \cos\delta) + \sin 2\alpha(\cos 2\phi \sin 2\phi(1 - \cos\delta))]$, $\boldsymbol{m}_{13} = \frac{1}{2}[\cos 2\alpha(\cos 2\phi \sin 2\phi(1 - \cos\delta)) + \sin 2\alpha(\sin^2\phi + \cos^2 2\phi \cos\delta)]$, and $\boldsymbol{m}_{14} = \frac{1}{2}[-\cos 2\alpha \sin 2\phi \sin\delta + \sin 2\alpha(\cos 2\phi \sin\delta)]$, thus the intensities (hereafter, $\bar{\boldsymbol{I}}_{\alpha,\phi,\delta}$) detected in the two spectropolarimeter cameras can be simply expressed as

$$\bar{\boldsymbol{I}}_{\alpha,\phi,\delta} = \frac{1}{2}\Big[I + \frac{1}{2}(Q\cos 2\alpha + U\sin 2\alpha)(1 + \cos\delta) + \sin\delta\sin(2\alpha - 2\phi)V$$

$$+ \frac{1}{2}(1-\cos\delta)\Big((Q\cos 2\alpha - U\sin 2\alpha)\cos 4\phi + (Q\sin 2\alpha + U\cos 2\alpha)\sin 4\phi\Big)\Big],\Bigg(\quad (2)$$

where α is the direction of the principal axis of the polarization analyzer installed on each channel with respect to the X-axis of the mechanical coordinates (Figure 3). Hence, $\alpha = 90°$ and $\alpha = 0°$ for channel 1 and 2, respectively. δ is the phase retardation of the waveplate, and ϕ is the rotation angle of the PMU (i.e., the rotation angle of the principal axis of the waveplate with respect to the X-axis of the mechanical coordinates).

The PMU performs a full rotation every 3.2 s in a clockwise direction as viewed from the entrance aperture of CLASP2. The spectropolarimeter cameras are synchronized with the PMU, acquiring 16 exposures per rotation. The PMU sends the first trigger signal to the spectropolarimeter cameras at $\phi = 0°$, and then sends additional trigger signals to the spectropolarimeter cameras every 0.2 seconds, corresponding to a PMU rotation angle of 22.5° between trigger events. The sensors are frame transfer CCDs with no mechanical shutter. When the trigger signal is received, the contents of the imaging array is transferred to the readout array **in about 3.2 ms**; this starts the next exposure in the imaging array while the readout array is read out. **The CLASP2 data has been corrected for frame transfer image smear based on Ruyten (1999). For the slit-jaw data, the entire CCD area is read out and a full smear correction can be performed. For the spectropolarimetric data, only a region of interest in the middle part of the CCD area is read out. The information in the outer parts is lost, but those regions still contribute to the image smear contamination. This was mitigated by linearly extrapolating the shape of the spectrum on both the red and the blue end in each pixel column, and calculating the image smear contamination based on this extrapolation.** Thus, the signals recorded by the two cameras ($D_{ti,1}$ for channel 1 and $D_{ti,2}$ for channel 2) can be expressed as the integral of Equation 2 with respect to the rotation angle, ϕ, of the PMU at each exposure:

$$\begin{aligned} D_{ti,1} &= \int_{\phi_{ai}}^{\phi_{bi}} \bar{\boldsymbol{I}}_{\alpha=90°,\phi,\delta}\, d\phi \\ &= \frac{1}{2}\Big[I - \Big(\frac{1}{2}(1+\cos\delta) + \frac{1}{\pi}(1-\cos\delta)(\sin 4\phi_{bi} - \sin 4\phi_{ai})\Big)Q \\ &+ \Big(\frac{1}{\pi}(1-\cos\delta)(\cos 4\phi_{bi} - \cos 4\phi_{ai})\Big)U \\ &- \frac{4}{\pi}\sin\delta(\cos 2\phi_{bi} - \cos 2\phi_{ai})V\Big] \end{aligned} \quad (3)$$

and

$$D_{ti,2} = \int_{\phi_{ai}}^{\phi_{bi}} \bar{\boldsymbol{I}}_{\alpha=0°,\phi,\delta}\, d\phi$$

Table 1. Observed signals in **the** two spectropolarimeter cameras **during half PMU rotation.** a_0, a_1, b, c_1, and c_2 indicate the modulation coefficients with **a** phase retardation of 234°.

Exposure	$D_{ti,channel1}$	$D_{ti,channel2}$
$t1_{(\phi=0°-22.5°)}$	$\frac{1}{2}[I-(a_0+a_1)Q-bU-c_1V]$	$\frac{1}{2}[I+(a_0+a_1)Q+bU+c_1V]$
$t2_{(\phi=22.5°-45.0°)}$	$\frac{1}{2}[I-(a_0-a_1)Q-bU-c_2V]$	$\frac{1}{2}[I+(a_0-a1)Q+bU+c_2V]$
$t3_{(\phi=45.0°-67.5°)}$	$\frac{1}{2}[I-(a_0-a_1)Q+bU-c_2V]$	$\frac{1}{2}[I+(a_0-a_1)Q-bU+c_2V]$
$t4_{(\phi=67.5°-90.0°)}$	$\frac{1}{2}[I-(a_0+a_1)Q+bU-c_1V]$	$\frac{1}{2}[I+(a_0+a_1)Q-bU+c_1V]$
$t5_{(\phi=112.5°-90.0°)}$	$\frac{1}{2}[I-(a_0+a_1)Q-bU+c_1V]$	$\frac{1}{2}[I+(a_0+a_1)Q+bU-c_1V]$
$t6_{(\phi=135.0°-112.5°)}$	$\frac{1}{2}[I-(a_0-a_1)Q-bU+c_2V]$	$\frac{1}{2}[I+(a_0-a_1)Q+bU-c_2V]$
$t7_{(\phi=157.5°-135.0°)}$	$\frac{1}{2}[I-(a_0-a_1)Q+bU+c_2V]$	$\frac{1}{2}[I+(a_0-a_1)Q-bU-c_2V]$
$t8_{(\phi=180.0°-157.5°)}$	$\frac{1}{2}[I-(a_0+a_1)Q+bU+c_1V]$	$\frac{1}{2}[I+(a_0+a_1)Q-bU-c_1V]$

$$
\begin{aligned}
&= \frac{1}{2}\Big[I+\Big(\cancel{\frac{1}{2}}(1+\cos\delta)+\frac{1}{\pi}(1-\cos\delta)(\sin 4\phi_{bi}-\sin 4\phi_{ai})\Big)Q\\
&- \Big(\frac{1}{\pi}(1-\cos\delta)(\cos 4\phi_{bi}-\cos 4\phi_{ai})\Big)U\\
&+ \frac{4}{\pi}\sin\delta(\cos 2\phi_{bi}-\cos 2\phi_{ai})V\Big] \qquad (4)
\end{aligned}
$$

where i indicates the i^{th} exposure, and ϕ_{ai} and ϕ_{bi} represent the rotation angles of the PMU at the beginning and end of the i^{th} exposure (e.g., $\phi_{a1}=0°$ and $\phi_{b1}=22.5°$), respectively.

The observed signals in two channels can be simply expressed as a function of each exposure, which is shown in Table 1. The terms a_0, a_1, b, c_1, and c_2 shown in the table represent the modulation coefficients $a_0=\frac{1}{2}(1-\cos\delta)$, $a_1=\frac{1}{\pi}(1-\cos\delta)(\sin 4\phi_{bi}-\sin 4\phi_{ai})$, $b=\frac{1}{\pi}(1-\cos\delta)(\cos 4\phi_{bi}-\cos 4\phi_{ai})$, $c_1=\frac{4}{\pi}\sin\delta(\cos 2\phi_{bi}-\cos 2\phi_{ai})$, and $c_2=\frac{4}{\pi}\sin\delta(\cos 2\phi_{bi}-\cos 2\phi_{ai})$.

3.3. Demodulation

First we demodulate the Stokes signals assuming a wavelength-constant phase retardation of 234° and an ideal system, that is, the perfectly-know position angles of PMU and polarizers (i.e., $a_0=0.206$, $a_1=0.505$, $b=0.505$, $c_1=0.302$, and $c_2=0.728$). Then we compensate the difference from the assumption for the true system by applying the response matrix (Section 3.4).

Demodulation is performed to derive the Stokes signals (Q'/I', U'/I', and V'/I') from the integrated modulated intensities shown in Table 1 using the following equations:

$$
\pm\frac{(-D_{t1}+D_{t2}+D_{t3}-D_{t4}-D_{t5}+D_{t6}+D_{t7}-D_{t8})}{(D_{t1}+D_{t2}+D_{t3}+D_{t4}+D_{t5}+D_{t6}+D_{t7}+D_{t8})}=\frac{D_Q}{D_T}
$$

$$\frac{Q'}{I'} = \frac{D_Q}{a_1 D_T \pm a_0 D_Q} \tag{5}$$

$$\pm \frac{(-D_{t2} + D_{t3} + D_{t4} - D_{t5} - D_{t6} + D_{t7} + D_{t8} - D_{t9})}{(D_{t2} + D_{t3} + D_{t4} + D_{t5} + D_{t6} + D_{t7} + D_{t8} + D_{t9})} = \frac{D_U}{D_T}$$

$$\frac{U'}{I'} = \frac{D_U}{a_1 D_T \pm a_0 D_Q} \tag{6}$$

$$\pm \frac{(-D_{t3} - D_{t4} + D_{t5} + D_{t6} + D_{t7} + D_{t8} - D_{t9} - D_{t10})}{(D_{t3} + D_{t4} + D_{t5} + D_{t6} + D_{t7} + D_{t8} + D_{t9} + D_{t10})} = \frac{D_V}{D_T}$$

$$\frac{V'}{I'} = \frac{\frac{2a_1}{c_1+c_2} D_V}{a_1 D_T \pm a_0 D_Q}, \tag{7}$$

where D_{ti} is the integrated intensity at the i^{th} exposure (see, Equation 3 and 4). The '$\pm$' sign in each the equation corresponds to the demodulation equations of channel 1 (positive sign) and channel 2 (negative sign). We find that the $a_0 D_Q$ term in the denominator of Equations 5 – 7 has a significant influence if the incoming light is highly polarized. In particular, this term must be considered in the polarization calibration on the ground, since we use perfectly polarized light in our laboratory.

On the other hand, the demodulation equations for the observation data from the Sun can neglect the $a_0 D_Q$ term in the denominator ($a_1 D_T \gg a_0 D_Q$) and can be simply expressed as

$$\frac{Q'}{I'} = \frac{D_Q}{a_1 D_T}, \qquad \frac{U'}{I'} = \frac{D_U}{a_1 D_T}, \qquad \frac{V'}{I'} = \frac{2}{c_1 + c_2} \frac{D_V}{D_T}, \tag{8}$$

as the Stokes Q signal (as well as U and V) is significantly smaller than the Stokes I signal.

3.4. Requirements for the Accuracy of Polarization Calibration

We verify the polarization characteristics of CLASP2 by determining the response matrix $\boldsymbol{X}$ (Elmore, 1990; Ichimoto et al., 2008);

$$\boldsymbol{S'} = \boldsymbol{X}\boldsymbol{S} = \begin{pmatrix} I' \\ Q' \\ U' \\ V' \end{pmatrix} = \begin{pmatrix} 1 & \boldsymbol{x}_{12} & \boldsymbol{x}_{13} & \boldsymbol{x}_{14} \\ \boldsymbol{x}_{21} & \boldsymbol{x}_{22} & \boldsymbol{x}_{23} & \boldsymbol{x}_{24} \\ \boldsymbol{x}_{31} & \boldsymbol{x}_{32} & \boldsymbol{x}_{33} & \boldsymbol{x}_{34} \\ \boldsymbol{x}_{41} & \boldsymbol{x}_{42} & \boldsymbol{x}_{43} & \boldsymbol{x}_{44} \end{pmatrix} \begin{pmatrix} I \\ Q \\ U \\ V \end{pmatrix}, \tag{9}$$

where $\boldsymbol{S'}$ and $\boldsymbol{S}$ are the demodulated and incident Stokes vectors. The response matrix $\boldsymbol{X}$ can be rewritten by normalizing to the Stokes $I' = 1 + q\boldsymbol{x}_{12} + u\boldsymbol{x}_{13} +$

$v\boldsymbol{x}_{14}$, which is given by

$$\begin{pmatrix} Q'/I' \\ U'/I' \\ V'/I' \end{pmatrix} = \begin{pmatrix} q' \\ u' \\ v' \end{pmatrix} = \frac{\begin{pmatrix} \boldsymbol{x}_{21} & \boldsymbol{x}_{22} & \boldsymbol{x}_{23} & \boldsymbol{x}_{24} \\ \boldsymbol{x}_{31} & \boldsymbol{x}_{32} & \boldsymbol{x}_{33} & \boldsymbol{x}_{34} \\ \boldsymbol{x}_{41} & \boldsymbol{x}_{42} & \boldsymbol{x}_{43} & \boldsymbol{x}_{44} \end{pmatrix} \begin{pmatrix} 1 \\ q \\ u \\ v \end{pmatrix}}{1 + q\boldsymbol{x}_{12} + u\boldsymbol{x}_{13} + v\boldsymbol{x}_{14}}, \tag{10}$$

where q, u, and v are Q/I, U/I, and V/I, respectively. The elements of $\boldsymbol{x}_{12}$, $\boldsymbol{x}_{13}$, $\boldsymbol{x}_{14}$, $\boldsymbol{x}_{22}$, $\boldsymbol{x}_{33}$, and $\boldsymbol{x}_{44}$ represent the scale factors that change the degree of measured polarization. The elements of $\boldsymbol{x}_{12}$, $\boldsymbol{x}_{13}$, and $\boldsymbol{x}_{14}$ are also interpreted as the Q, U, and V to I crosstalk, and are negligible in solar observations, where generally $I \gg Q$, U, and V. However, they have a significant influence if the degree of polarization is close to 100% such as in the polarization calibration (Section 5). The other elements of $\boldsymbol{x}$ are crosstalk among the polarization signals, e.g., $\boldsymbol{x}_{23}$ for $U \rightarrow Q$ crosstalk and $\boldsymbol{x}_{32}$ for $Q \rightarrow U$ crosstalk. Additionally, $\boldsymbol{x}_{21}$, $\boldsymbol{x}_{31}$, and $\boldsymbol{x}_{41}$ represent a crosstalk from intensity to the polarization signal, i.e., spurious polarization terms. In the ideal case, $\boldsymbol{X}$ is a 4×4 identity matrix (i.e., unity scale factor and no crosstalk).

Our polarization calibration implementation aims to determine the response matrix of CLASP2 within the required tolerance. The final goal of CLASP2 is to achieve a polarization accuracy of 0.1% at 3σ level. As described in Appendix A, the main source of polarization errors is photon noise ($\sigma_{photon} \approx 0.02\%$) and measurement errors in the polarization calibration. The latter consists of the measurement errors associated to the spurious polarization term (ϵ_s), scale factors (ϵ_a), and crosstalk (ϵ_c) in the response matrix. By allocating 0.017% to ϵ_s (Ishikawa et al., 2014) as well as 0.0137% to ϵ_a and ϵ_c, the total polarization error is $\sigma = \sqrt{\sigma_{photon}^2 + \epsilon_s^2 + \epsilon_a^2 + \epsilon_c^2} \approx 0.033\%$.

The required tolerance of the scale factor and crosstalk terms can be estimated by dividing ϵ_a and ϵ_c by the maximum polarization degree expected for solar observations (Ichimoto et al., 2008). The maximum polarization degree is about 3% for the linear (p_l) and circular (p_v) polarizations (Alsina Ballester, Belluzzi, and Trujillo Bueno, 2016). Four terms of the scale factors and two terms of the crosstalk contribute to each fractional polarization of Q'/I', U'/I', and V'/I'. Hence, the required tolerance for each elements of $\boldsymbol{X}$ is

$$\begin{aligned} |\Delta\boldsymbol{X}| \;&\leq\; \begin{pmatrix} - & \epsilon_a/p_l/\sqrt{4} & \epsilon_a/p_l/\sqrt{4} & \epsilon_a/p_v/\sqrt{4} \\ \epsilon_s & \epsilon_a/p_l/\sqrt{4} & \epsilon_c/p_l/\sqrt{2} & \epsilon_c/p_v/\sqrt{2} \\ \epsilon_s & \epsilon_c/p_l/\sqrt{2} & \epsilon_a/p_l/\sqrt{4} & \epsilon_c/p_v/\sqrt{2} \\ \epsilon_s & \epsilon_c/p_l/\sqrt{2} & \epsilon_c/p_l/\sqrt{2} & \epsilon_a/p_v/\sqrt{4} \end{pmatrix} \\ &= \begin{pmatrix} - & 0.00229 & 0.00229 & 0.00229 \\ 0.00017 & 0.00229 & 0.00325 & 0.00325 \\ 0.00017 & 0.00325 & 0.00229 & 0.00325 \\ 0.00017 & 0.00325 & 0.00325 & 0.00229 \end{pmatrix}. \end{aligned} \tag{11}$$

Table 2. Data from the pre-flight polarization calibration.

	Inputs	Orientation of the polarizer	Orientation of the quarter waveplate
Linearly polarized	$\pm Q$	0°, 90° or 180°, 270°	not installed
	$\pm U$	45°, 135° or 225°, 315°	not installed
Circularly polarized	$\pm V$	0° or 180°	45°, 135° or 225°, 315°
Un-polarized[1]	"un-polarized"	not installed	not installed

[1] "Un-polarized" light was obtained by removing the polarizer and the quarter waveplate in the light source chamber.

4. CLASP2 Polarization Calibration Strategy

The polarization calibration of CLASP2 was performed based on our experience with CLASP1 in the vacuum UV (VUV) spectral range (Giono et al., 2016, 2017) and following two steps. First, we determined the scale factor and the crosstalk terms from pre-flight data taken with a custom-made polarized light source at 280 nm in a laboratory (Section 5). To this end, the spurious polarization terms ($\boldsymbol{x}_{21}$, $\boldsymbol{x}_{31}$, and $\boldsymbol{x}_{41}$ in $\boldsymbol{X}$) are assumed to be zero. This is a reasonable assumption because we have confirmed with "un-polarized" light that the spurious polarization terms are too small to affect other terms such as the scale factor and crosstalk (Section 5.4). The measurement with "un-polarized" light is newly added in CLASP2 based on what we learned from the CLASP1 polarization calibration (Giono et al., 2016). Second, the spurious polarization terms were accurately determined by analyzing the in-flight data taken at the solar disk center for 15 seconds (Section 6). Note that, it is expected that the spatially averaged scattering polarization along the slit on the solar disk center is close to zero because of the symmetric illumination field (Giono et al., 2017).

5. Polarization Calibration Using Pre-flight Data

5.1. Test Configuration

The pre-flight polarization calibration was performed only for the spectropolarimeter. As the instrumental polarization caused by the telescope is negligibly small (see Appendix A.1), the response matrix measured for the spectropolarimeter, i.e., starting at the PMU location, can represent that of the entire CLASP2 instrument.

A custom-made UV light source was developed to supply the required polarization states around the 280 nm wavelength to the spectropolarimeter without the telescope. Figure 3 shows two different layouts of our light source vacuum chamber for linear and circular polarization inputs. The light source for the linear polarization input consists of a UV LED lamp, a MgF_2 lens for the focusing, and a linear polarizer. The UV LED lamp emits ultraviolet light ranging from 275 nm

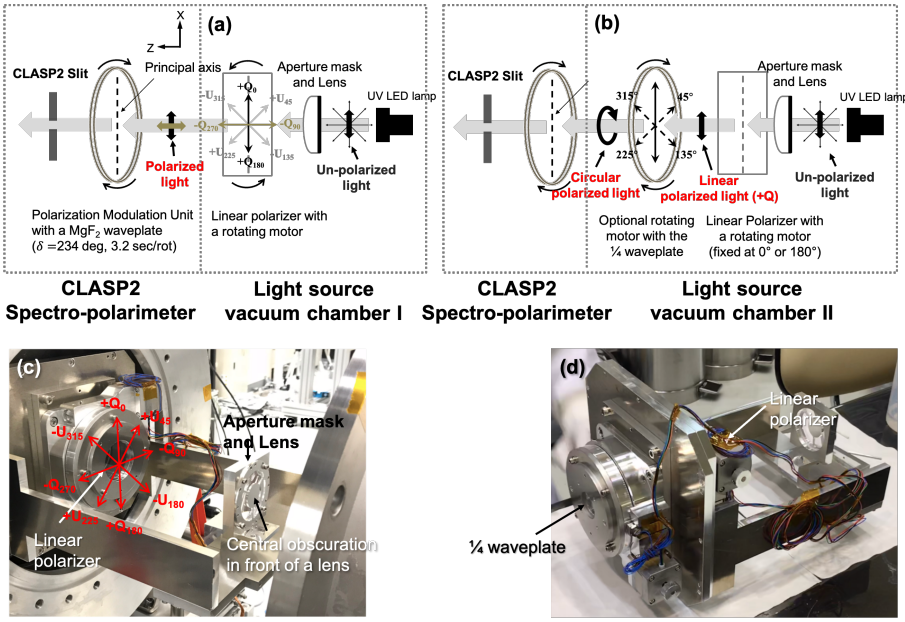

Figure 3. Schematic image of the custom-made light source system for (a) linear and (b) circular polarizations, using a UV LED lamp. The light source chamber is directly attached to the CLASP2 spectropolarimeter without the telescope during calibration. (c) and (d) show the inside of the light source chamber for the linear and the circular polarization inputs, respectively. The *red arrows* indicate the polarization coordinate system of CLASP2 as seen from the instrument entrance port.

to 285 nm with a full width at a half maximum of 12 nm. It is installed on a three-axis linear stage to adjust the lamp for positioning and focusing the UV light on the CLASP2 slit mirror. The focusing lens with an aperture mask ensures that output light from the light source system has the same F number (F/9.68) and beam pattern as the telescope. The linear polarizer is installed on a motorized rotational stage (0.0025°/step). The light source is additionally equipped with a quarter waveplate on another motorized rotational stage behind the linear polarizer of the aforementioned **design to obtain circularly polarized light.**

The red arrows marked in Figure 3 represent the polarization coordinate system of CLASP2 as defined in Section 3.1. Two data sets were obtained for the linear polarization inputs. One (hereafter, Dataset I) includes four orientations of the principal axis of the light source linear polarizer namely 0°, 45°, 90°, and 135°, defined as $+Q_{0°}$, $+U_{45°}$, $-Q_{90°}$, and $-U_{135°}$. The other (hereafter, Dataset II) includes $+Q_{180°}$, $+U_{225°}$, $-Q_{270°}$, and $-U_{315°}$ corresponding to the second half rotation of the polarizer. The polarization error caused by non-uniformity of the linear polarizer installed inside the light source chamber can be suppressed by combining these two datasets. For the circular polarization input, four datasets (hereafter, Dataset III) are used with the orientations of a principal axis of the quarter waveplate, which converts linear polarization to circular polarization at 45° and 135° or 225° and 315°. The orientation of the linear polarizer located upstream of the quarter waveplate was fixed at 0°

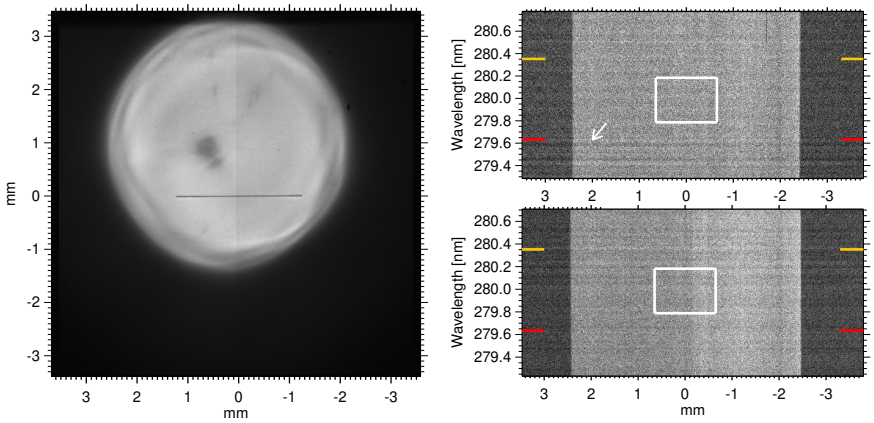

Figure 4. Images captured by the SJ camera (*left*) and the spectropolarimeter cameras staking all exposures (*right top*: channel 1 and *right bottom*: channel 2) during the pre-flight polarization calibration. The spectropolarimeter images accumulated all exposures, reducing striated patterns and noise. They were taken using a custom-made polarization light source system based on a UV LED lamp. The wavelength axis of the spectra in the spectropolarimeter images is defined using the data recorded during the alignment of the spectropolarimeter, in which the sharp Mg II h and k lines emitted by the Mg hollow cathode lamp are examined (Song et al., 2018). The *orange* and *red solid lines* in the spectropolarimeter images represent the positions of the Mg II h and k lines, respectively. The *white arrow* indicates one of the stripe patterns likely due to electrical noise. The *white boxes* represent the regions where we averaged to comupte the response matrix.

or 180°. These datasets can suppress polarization errors due to not only the non-uniformity of the linear polarizer but also that of the quarter waveplate, i.e., rotation angle error, thickness difference, flatness of the surface, and the contamination on the surface (Giono et al., 2016). Table 2 lists the summary of the data taken on the ground.

5.2. Pre-flight Data and Data Analysis

The desired polarized light emitted from the light source system is focused directly on the CLASP2 slit mirror. At the best focus position, the beam size of the UV LED lamp is about 5 mm, which is sufficiently large to cover the entire length of the spectropolarimeter slit (2.5 mm). The illuminated region on the slit was adjusted to avoid a dimmed region detected near the center of the beam spot (see left panel in Figure 4).

The two rightmost panels of Figure 4 show images captured by the two spectropolarimeter cameras during the pre-flight polarization calibration. The spectra of the UV LED lamp completely covers the required spectral window of 279.985 ± 0.45 nm. The orange and red lines in Figure 4 indicate the wavelength positions of the Mg II h and k lines, respectively.

Several stripe patterns can be seen in the spectropolarimeter images along the spatial direction, which may be caused by electrical noise. The width of each stripe pattern is about 0.05 nm (10 pixels), and the maximum fluctuation of the stripe noise is sometimes comparable to the minimum value of the modulated

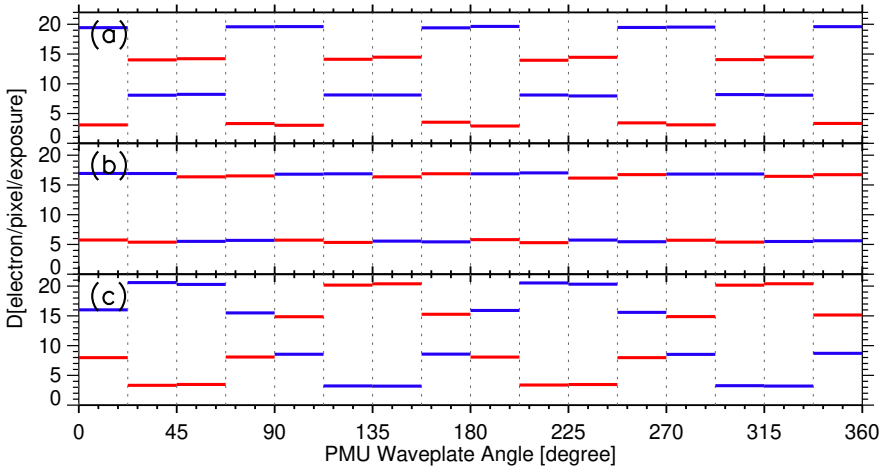

Figure 5. Modulated intensities as a function of the rotation angles of the PMU. They are obtained from (a) +Q, (b) +U, and (c) +V polarized inputs emitted from the light source system. The *red* and *blue solid lines* represent the intensity integrated every 22.5° PMU rotation (*dashed lines*) on channel 1 and 2, respectively.

signal. We reduced the influence of the stripe noise by averaging the signals detected outside the slit and subtracting them at the row-wise level in each spectropolarimeter image. Nevertheless, in the final processed spectral images, we find that the residual fixed stripe patterns weakly remain (e.g., white arrow in Figure 4).

The photon noise is reduced to 10^{-4} by stacking data recorded during 290 PMU rotations and accumulating 100 (spatial) × 80 (spectral) pixels. In particular, the summation of 80 pixels in the spectral direction can significantly suppress the influence of residual fixed patterns that can remain even after removing the stripe noise patterns. We derived the demodulated polarization signals around the 279.985 nm wavelength, which is the center of the required CLASP2 spectral window.

Figure 5 shows the registered modulated intensities (see Equations 3 and 4) as a function of the PMU rotation angles for $+Q$ (top pannel), $+U$ (middle pannel), and $+V$ (bottom pannel) inputs. The red and blue horizontal lines represent channel 1 and 2 signals, respectively. These are integrated every 22.5° PMU rotation. The maximum and minimum signal of each modulation is approximately 20 and 3 electrons/pixel/exposure, respectively. Notably, a non-negligible phase shift of the modulation at the linearly polarized input (Cases a and b in Figure 5) exists, especially on channel 1. Note that, the two consecutive integrated signals around each modulation peak should be the same for an ideal polarization modulation, but it is not the case for channel 1 due to the polarization characteristics of the instrument.

Table 3. Demodulated polarization signals (q', u', and v') derived from both channels at the wavelength of 279.985 nm.

#	Inputs	Channel 1			Channel 2		
		q'	u'	v'	q'	u'	v'
I[1]	$+Q_{0^\circ}$[2]	+0.99286	+0.03372	+0.00807	+0.98378	+0.00327	−0.00119
	$-Q_{90^\circ}$	−0.97651	−0.03349	−0.00292	−0.99756	−0.00219	+0.00554
	$+U_{45^\circ}$	−0.03483	+0.99178	+0.00485	−0.00367	+0.99784	+0.00503
	$-U_{135^\circ}$	+0.03358	−0.98166	+0.00545	+0.00272	−0.98478	+0.00579
	$+V_{135^\circ}$[3]	+0.02850	+0.01334	+0.98650	+0.02979	+0.01208	+0.99371
	$-V_{45^\circ}$	+0.01037	+0.01714	−0.98953	+0.01009	+0.01765	−0.98463
II[1]	$+Q_{180^\circ}$	+0.99492	+0.03510	+0.01345	+0.98435	+0.00322	+0.00456
	$-Q_{270^\circ}$	−0.97794	−0.03441	−0.00540	−0.99801	−0.00387	+0.00362
	$+U_{225^\circ}$	−0.03493	+0.99154	+0.00623	−0.00412	+0.99858	+0.00739
	$-U_{315^\circ}$	+0.03445	−0.97997	−0.00188	+0.00351	−0.98375	−0.00224
	$+V_{315^\circ}$	+0.02832	+0.01491	+0.98508	+0.02883	+0.01316	+0.99479
	$-V_{225^\circ}$	+0.00951	+0.01855	−0.98741	+0.00924	+0.01863	−0.98437

[1]#I and #II indicate the Datasets I and II, respectively.
[2]Subscript θ in $\pm Q_\theta$ and $\pm U_\theta$ is the angle of the linear polarizer installed inside the light source chamber.
[3]Subscript θ in $\pm V_\theta$ is the angle of the quarter waveplate installed inside the light source chamber, when the linear polarizer angle inside the light source chamber is fixed at 0°.

5.3. Demodulated Polarization Signals

Table 3 lists the demodulated polarization signals of q', u', and v' determined at the wavelength of 279.985 nm for each channel. For convenience, q', u', and v' obtained from ±Q, ±U, and ±V inputs, respectively, are designated as "major terms", whereas others (e.g., u' and v' determined from ±Q inputs) are designated as "minor terms". Notably, the major terms determined from the two datasets are all close to 1, and the minor terms are almost 0. Here, we notice a difference of approximately 10^{-4} to 10^{-3} in the values of major terms between Datasets I and II (e.g., $+Q_0$ and $+Q_{180}$ inputs). Such a difference suggests that the polarization state of the light source system depends on the orientation of the linear polarizer installed inside the light source chamber. The final demodulated polarization signals of CLASP2 are determined by averaging the demodulated polarization signals obtained from these two datasets. This is expected to resolve the polarization errors caused by the non-uniformity of the linear polarizer in the light source system (Giono et al., 2016).

Most of the minor terms determined from the linearly polarized inputs ($\pm Q$ and $\pm U$ inputs) are at the $\approx 10^{-3}$ level, excluding two terms of channel 1. Note that, the demodulated q' signal determined from $\pm U$ inputs and u' signal from $\pm Q$ inputs of channel 1 are ≈ 0.03. These non-negligible minor terms in channel 1 are consistent with the deviation from the ideal modulation of channel 1, as discussed at the end of Section 5.2. We find from the table that minor terms of both channels measured from the $\pm V$ inputs are larger than 0.009 (maximum value ≈ 0.029) and are all positive. This behavior, common to both channels,

Table 4. Demodulated polarization signals of q', u', and v' determined using the "un-polarized" input. Dataset I, Dataset II, and Dataset III represent the three datasets obtained at different times on the same day. **All signals are expressed like the power** -4 **of** 10**.**

Channel	Stokes signal	Dataset ($\times 10^{-4}$)			Mean ($\times 10^{-4}$)
		I	II	III	
1	q'	$+3.0$	$+3.6$	$+1.2$	$+2.6$
	u'	-1.8	$+0.2$	-1.1	-0.9
	v'	-10.0	-8.7	-12.0	-10.0
2	q'	$+1.0$	$+1.5$	0	$+0.8$
	u'	-7.0	-4.9	-7.2	-6.4
	v'	-12.0	-9.8	-13.0	-11.0

can be explained by the imperfectness of the light source (see Appendix B.1). Such an imperfectness of the light source is also manifested in contamination of the linearly polarized input beam (Appendix B.2). In fact, the relatively large v' signal of $\approx 10^{-2}$ level is detected from $+Q$ input in the channel 1.

5.4. Demodulated Polarization Signals with "Un-polarized" Light

After the pre-flight polarization calibration, we obtained several datasets using "un-polarized" light to determine the spurious polarization terms of both channels. The "un-polarized" light mentioned here indicates the light from the UV LED lamp without any polarization units inside the light source vacuum chamber, such as the linear polarizer and the quarter waveplate. However, the "un-polarized" light used here on the ground does not mean perfectly un-polarized light in nature (e.g., the UV LED lamp itself could produce an unexpected polarization signal). Nevertheless, an upper limit can be set on the spurious polarization (see Table 4)

Table 4 lists the demodulated signals measured from the data taken by "un-polarized" light; q' and u' signals are $< 10^{-4}$ and v' signal is $< 10^{-3}$. Assuming that our "un-polarized" light is perfectly un-polarized, these signals are interpreted as the spurious polarization terms corresponding to $\boldsymbol{x}_{21}$, $\boldsymbol{x}_{31}$, and $\boldsymbol{x}_{41}$, as defined in Section 3.4.

We investigated the variations in the scale factor and crosstalk of the response matrix by substituting signals of the spurious polarization shown in Table 4 into Equations 15 – 25. The changes of the diagonal elements and the crosstalk terms are of the order of 10^{-6} at maximum, which is negligibly small. This implies that the spurious polarization is sufficiently small and does not significantly affect the other terms in the response matrix. Therefore, the spurious polarization terms are assumed zero for analyzing the pre-flight data. Note that the spurious polarization terms for the final response matrix will be accurately determined using the in-flight data (see Section 6).

5.5. Determination of Response Matrix Elements

The demodulated polarization signals of each Stokes vector are given by

$$q' = \frac{x_{21} + qx_{22} + ux_{23} + vx_{24}}{1 + qx_{12} + ux_{13} + vx_{14}} \tag{12}$$

$$u' = \frac{x_{31} + qx_{32} + ux_{33} + vx_{34}}{1 + qx_{12} + ux_{13} + vx_{14}} \tag{13}$$

$$v' = \frac{x_{41} + qx_{42} + ux_{43} + vx_{44}}{1 + qx_{12} + ux_{13} + vx_{14}}. \tag{14}$$

The elements of the response matrix for CLASP2 are estimated by assuming that the input beams emitted from the light source system is fully polarized. Then, the polarization states of each input defined as $\pm Q$, $\pm U$, and $\pm V$ can be expressed in the Stokes vector forms of $(1,q,u,v)^\top=(1,\pm1,0,0)^\top$, $(1,0,\pm1,0)^\top$, and $(1,0,0,\pm1)^\top$. Then, Equations 12 – 14 can be simplified to

$$[q']_{\pm Q} = \frac{\boldsymbol{x}_{21} \pm \boldsymbol{x}_{22}}{1 \pm \boldsymbol{x}_{12}}, \quad [u']_{\pm Q} = \frac{\boldsymbol{x}_{31} \pm \boldsymbol{x}_{32}}{1 \pm \boldsymbol{x}_{12}}, \quad [v']_{\pm Q} = \frac{\boldsymbol{x}_{41} \pm \boldsymbol{x}_{42}}{1 \pm \boldsymbol{x}_{12}} \tag{15}$$

$$[u']_{\pm U} = \frac{\boldsymbol{x}_{31} \pm \boldsymbol{x}_{33}}{1 \pm \boldsymbol{x}_{13}}, \quad [v']_{\pm U} = \frac{\boldsymbol{x}_{41} \pm \boldsymbol{x}_{43}}{1 \pm \boldsymbol{x}_{13}}, \quad [q']_{\pm U} = \frac{\boldsymbol{x}_{21} \pm \boldsymbol{x}_{23}}{1 \pm \boldsymbol{x}_{13}} \tag{16}$$

$$[v']_{\pm V} = \frac{\boldsymbol{x}_{41} \pm \boldsymbol{x}_{44}}{1 \pm \boldsymbol{x}_{14}}, \quad [q']_{\pm V} = \frac{\boldsymbol{x}_{21} \pm \boldsymbol{x}_{24}}{1 \pm \boldsymbol{x}_{14}}, \quad [u']_{\pm V} = \frac{\boldsymbol{x}_{31} \pm \boldsymbol{x}_{34}}{1 \pm \boldsymbol{x}_{14}}. \tag{17}$$

The spurious polarization terms ($\boldsymbol{x}_{21}$, $\boldsymbol{x}_{31}$, and $\boldsymbol{x}_{41}$) are assumed as zero (see Section 4 and Section 5.4) to derive each element of the CLASP2 response matrix. Under such assumptions, the scale factors ($\boldsymbol{x}_{22}$, $\boldsymbol{x}_{33}$, $\boldsymbol{x}_{44}$, $\boldsymbol{x}_{12}$, $\boldsymbol{x}_{13}$, and $\boldsymbol{x}_{14}$) are derived using the equations for "major terms" ($[q']_{\pm Q}$, $[u']_{\pm U}$, and $[v']_{\pm V}$ in Equations 15 – 17). They are expressed as

$$\boldsymbol{x}_{22} = \frac{2\,[q']_{+Q}\,[q']_{-Q}}{[q']_{-Q} - [q']_{+Q}}, \quad \boldsymbol{x}_{33} = \frac{2\,[u']_{+U}\,[u']_{-U}}{[u']_{-U} - [u']_{+U}}, \quad \boldsymbol{x}_{44} = \frac{2\,[v']_{+V}\,[v']_{-V}}{[v']_{-V} - [v']_{+V}} \tag{18}$$

$$\boldsymbol{x}_{12} = \frac{[q']_{-Q} + [q']_{+Q}}{[q']_{-Q} - [q']_{+Q}}, \quad \boldsymbol{x}_{13} = \frac{[u']_{-U} + [u']_{+U}}{[u']_{-U} - [u']_{+U}}, \quad \boldsymbol{x}_{14} = \frac{[v']_{-V} + [v']_{+V}}{[v']_{-V} - [v']_{+V}}. \tag{19}$$

Next, all crosstalk terms are determined by substituting the obtained values of $\boldsymbol{x}_{12}$, $\boldsymbol{x}_{13}$, and $\boldsymbol{x}_{14}$ into the equations for "minor terms". First, the elements of the $Q \leftrightarrow U$ crosstalk ($\boldsymbol{x}_{23}$ and $\boldsymbol{x}_{32}$) are estimated by

$$\boldsymbol{x}_{23} = \frac{1}{2}\Big[\Big((1 + \boldsymbol{x}_{13})[q']_{+U} - (1 - \boldsymbol{x}_{13})[q']_{-U}\Big]\Big(\tag{20}$$

and

$$\boldsymbol{x}_{32} = \frac{1}{2}\Big[(1+\boldsymbol{x}_{12})[u']_{+Q} - (1-\boldsymbol{x}_{12})[u']_{-Q}\Big], \tag{21}$$

which are derived from the equations of $[q']_{\pm U}$ and $[u']_{\pm Q}$ in Equations 15 and 16. Second, we consider the elements of $V \rightarrow Q$ or U crosstalk ($\boldsymbol{x}_{24}$ and $\boldsymbol{x}_{34}$). They are expressed as

$$\boldsymbol{x}_{24} = \frac{1}{2}\Big[(1+\boldsymbol{x}_{14})[q']_{+V} - (1-\boldsymbol{x}_{14})[q']_{-V}\Big] \tag{22}$$

and

$$\boldsymbol{x}_{34} = \frac{1}{2}\Big[(1+\boldsymbol{x}_{14})[u']_{+V} - (1-\boldsymbol{x}_{14})[u']_{-V}\Big], \tag{23}$$

which are derived from the equations of $[q']_{\pm V}$ and $[u']_{\pm V}$ in Equations 17. Finally, the elements of Q or $U \rightarrow V$ crosstalk are determined by

$$\boldsymbol{x}_{42} = \frac{1}{2}\Big[(1+\boldsymbol{x}_{12})[v']_{+Q} - (1-\boldsymbol{x}_{12})[v']_{-Q}\Big] \tag{24}$$

and

$$\boldsymbol{x}_{43} = \frac{1}{2}\Big[(1+\boldsymbol{x}_{13})[v']_{+U} - (1-\boldsymbol{x}_{13})[v']_{-U}\Big], \tag{25}$$

which are derived from the equations of $[v']_{\pm Q}$ and $[v']_{\pm U}$ in Equations 15 and 16.

On the other hand, if the input beams are not completely polarized, q and u contamination in $\pm V$ inputs (Appendix B.1) as well as v contamination in $\pm Q$ and $\pm U$ inputs (Appendix B.2) can be considered. However, even in this case, we confirmed that it does not affect the determination of each element of the response matrix (see Appendix B).

5.6. Representative Response Matrix

The measured response matrices ($\boldsymbol{X}$) of CLASP2 are

$$\boldsymbol{X}_1 = \begin{pmatrix} 1 & -0.00846 & -0.00550 & -0.00025 \\ 0 & +0.98549 & -0.03445 & +0.00682 \\ 0 & +0.03418 & +0.98621 & -0.00111 \\ 0 & +0.00743 & +0.00186 & +0.98647 \end{pmatrix} \tag{26}$$

and

$$\boldsymbol{X}_2 = \begin{pmatrix} 1 & +0.00692 & -0.00704 & -0.00636 \\ 0 & +0.99088 & -0.00350 & +0.00693 \\ 0 & +0.00314 & +0.99119 & -0.00168 \\ 0 & -0.00143 & +0.00219 & +0.98655 \end{pmatrix} \tag{27}$$

on channel 1 ($\boldsymbol{X}_1$) and channel 2 ($\boldsymbol{X}_2$), respectively. They are determined at the wavelength of 279.985 nm. Hereafter, they are called the representative response matrices of CLASP2 for convenience. The measured response matrix on each

channel is close to an ideal response matrix as the diagonal elements are close to 1 and other elements are close to 0 ($\approx 10^{-3}$).

One of the notable findings from the representative response matrices is that we can see relatively large Q↔U crosstalk on channel 1 as both the $|\boldsymbol{x}_{23}|$ and $|\boldsymbol{x}_{32}|$ are ≈ 0.034, which are approximately 10 times larger than other off-diagonal elements. The presence of such a non-negligible crosstalk, only seen in channel 1, indicates that a source possibly exists inside the instrument of channel 1. The similar value of $|\boldsymbol{x}_{23}|$ and $|\boldsymbol{x}_{32}|$ of ≈ 0.034 with the opposite signs is consistent with the misalignment of a principal axis of the polarization analyzer installed on channel 1 of $\Delta \approx 0.49°$. The angle of the principal axis with respect to the exterior that is our reference for the installation is not measured or guaranteed. Thus, such a relatively large internal misalignment can occur.

The other finding is that the diagonal elements $\boldsymbol{x}_{22}$, $\boldsymbol{x}_{33}$, and $\boldsymbol{x}_{44}$ determined for both channels are approximately 1.2 % smaller than unity. Several possibilities can cause deviations in both the light source system and CLASP2 as discussed below. The first possible source is the imperfection in the polarization degree of the input beam emitted from the light source system. As discussed in Appendix B.3, one of the measurements of the extinction ratio from the light source polarizer is consistent with this. However, it is not conclusive. The second source can be that the phase retardation is different from 234° that has been used for the demodulation. The phase retardation of 234° is determined based on our measurement of the birefringence of the MgF_2, and the measured error is $\approx \pm 1°$ around the 280 nm wavelength (Section 2.1). This error of $\pm 1°$ can lead to $\pm 1\%$ difference in the scale factor of the response matrix. However, the influence is opposite between linear and circular polarizations (i.e., v' becomes larger than 1 if q' and u' become less than 1). Finally, the influence of stray light, i.e., the contamination of un-polarized light needs examination. Outside of the slit in the spectral image, 1% stray light level is detected compared to the signal. However, it shows modulation (i.e., the level changes depending on the PMU rotation angles), which indicates that the stray light is also partially polarized. It indicates that the stray light can affect the error of the scale factor, but its contribution would be smaller than 1%.

5.7. Uncertainty of the Response Matrix

The uncertainty of the CLASP2 response matrix elements is measured by analyzing the repeatability of the data taken during eight consecutive days (four days for linear polarization measurements and four days for circular polarization measurements) from the ground-based experiments. We repeatedly obtained Dataset I, Dataset II, and Dataset III mentioned in Section 5.1 in a laboratory maintained at the similar temperature and humidity every day. Then, the uncertainty of the response matrix was derived using the stacking data taken during 290 PMU rotations. The measured uncertainties of channel 1 ($\Delta \boldsymbol{X}_1$) and 2 ($\Delta \boldsymbol{X}_2$) are

$$\Delta \boldsymbol{X}_1 = \pm \begin{pmatrix} 0 & 0.00153 & 0.00059 & 0.00229 \\ \# & 0.00156 & 0.00186 & 0.00265 \\ \# & 0.00226 & 0.00032 & 0.00156 \\ \# & \mathbf{0.00329} & 0.00064 & 0.00186 \end{pmatrix} \Bigg(\tag{28}$$

and

$$\Delta \boldsymbol{X}_2 = \pm \begin{pmatrix} 0 & 0.00083 & 0.00118 & 0.00074 \\ \# & 0.00106 & 0.00229 & 0.00309 \\ \# & \mathbf{0.00398} & 0.00080 & 0.00133 \\ \# & 0.00090 & 0.00079 & \mathbf{0.00384} \end{pmatrix}, \tag{29}$$

where the uncertainty of each element is determined by the peak-to-reference value. Here, the uncertainty of spurious polarization terms is denoted by '#', since the spurious polarization is set to zero for analyzing the pre-flight data. We find from $\Delta \boldsymbol{X}$s that most values of the evaluated uncertainty meet our required tolerance defined in Equation 11, while some do not (bold text in Equations 28 and 29). However, even if we include the element that is not satisfied with the tolerance, the uncertainty of the Stokes parameters derived by combining each element is smaller than the total tolerance of 0.45% ($\epsilon_a/P{=}\epsilon_c/P$ with $P = P_l = P_v$) for "scale factor" and "crosstalk". For example, the scale factor of V'/I' is contributed by $\boldsymbol{x}_{12}, \boldsymbol{x}_{13}, \boldsymbol{x}_{14}$, and $\boldsymbol{x}_{44}$; consequently, the total scale error of the Stokes V'/I' on channel 2 is $\sqrt{0.00384^2 + 0.00083^2 + 0.00118^2 + 0.00074^2} = 0.00417 = 0.42\%$. Similarly, the crosstalk of U'/I' is contributed by $\boldsymbol{x}_{32}$ and $\boldsymbol{x}_{34}$; therefore, the total crosstalk error of the Stokes U'/I' on channel 2 is $\sqrt{0.00398^2 + 0.00133^2} = 0.00419 = 0.42\%$.

5.8. Dependence of the Response Matrix Elements on Wavelength

Figure 6 shows the variations in the response matrix elements with wavelength within the range of the CLASP2 spectral window. Each element is measured at eight positions with a 0.15 nm wavelength interval along the spectral direction. To reduce the photon and electrical noise, we accumulated all the data taken during 290 PMU rotations and also summed 100 (spatial) × 80 (spectral) pixels around each of the selected wavelength positions. We find from the figure that all the elements change linearly with the wavelength. Thus, the variations in each response matrix element can be simplified to a linear equation ($\boldsymbol{x} = A\lambda + B$) that has a wavelength (λ) dependence; consequently, the wavelength-dependent response matrices on both channels are

$$\boldsymbol{X}_1 = \begin{pmatrix} 1 & +0.009\lambda - 0.009 & +0.002\lambda - 0.005 & -0.0003 \\ \# & +0.009\lambda + 0.985 & +0.008\lambda - 0.034 & +0.002\lambda + 0.007 \\ \# & -0.008\lambda + 0.034 & +0.009\lambda + 0.985 & -0.0012 \\ \# & +0.001\lambda + 0.007 & +0.0018 & -0.012\lambda + 0.987 \end{pmatrix}, \tag{30}$$

and

$$\boldsymbol{X}_2 = \begin{pmatrix} 1 & -0.008\lambda + 0.007 & -0.003\lambda - 0.007 & +0.001\lambda - 0.006 \\ \# & +0.009\lambda + 0.991 & +0.008\lambda - 0.003 & +0.002\lambda + 0.007 \\ \# & -0.008\lambda + 0.003 & +0.009\lambda + 0.991 & -0.0017 \\ \# & -0.0015 & +0.0021 & -0.012\lambda + 0.987 \end{pmatrix}. \tag{31}$$

Here, some elements, which are within our required tolerance across the entire wavelength of the CLASP2 spectral window, are set to a constant value of the

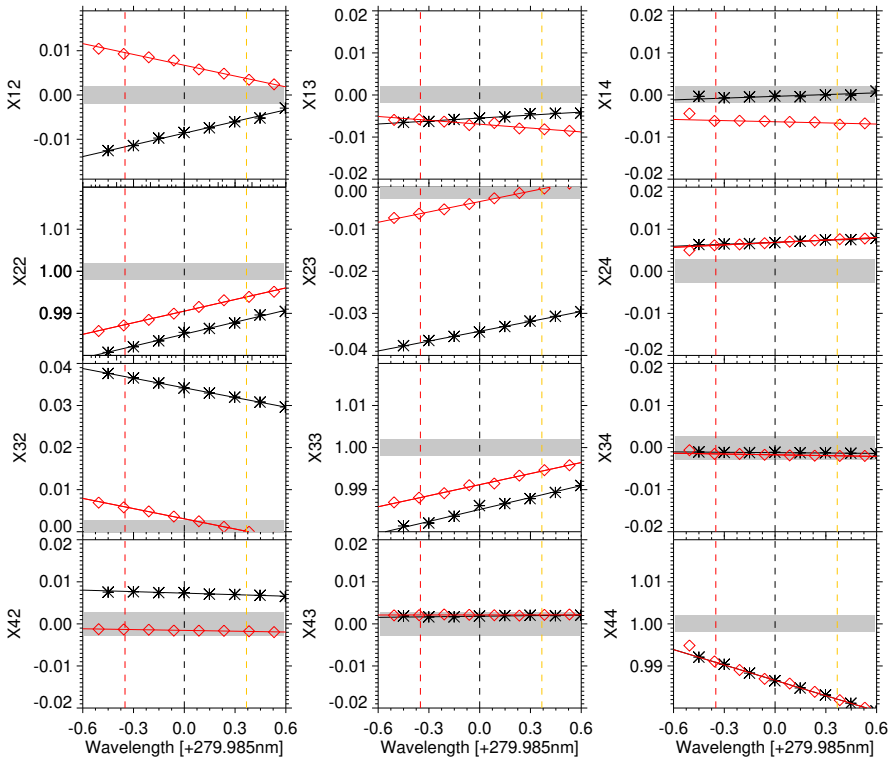

Figure 6. Variations in the response matrix elements with wavelength across the CLASP2 spectral window (centered at 280 nm). The *asterisk* and *diamond* represent the data points taken from channels 1 and 2, respectively. The *solid black* and *red lines* indicate the results of a linear fitting on each channel using the eight data points. Note that, the linear equations derived from the fitting results of each channel are showcased in Equations 30 and 31. The *gray color* represents a range of the required tolerance for each response matrix element. The wavelengths of the Mg II h and k lines are represented by the *vertical orange* and *red dashed lines*.

offset in each linear equation. Note that the maximum difference between both ends of the wavelength is ≈ 0.013 (e.g., $\boldsymbol{x}_{44}$ in Figure 6), which is not negligible. This suggests that the dependence of the response matrix on the wavelength should be considered in the final polarization correction.

6. Polarization Calibration Using In-flight Data

6.1. In-flight Data and Data Analysis

Following the strategy of the CLASP2 observations, we performed Sun-center observations ($\mu \approx 1$) for the first 15 seconds to confirm the polarization characteristics of CLASP2. The spatially averaged linear polarization caused by scattering at the quiet region is expected to be zero because of the symmetrical

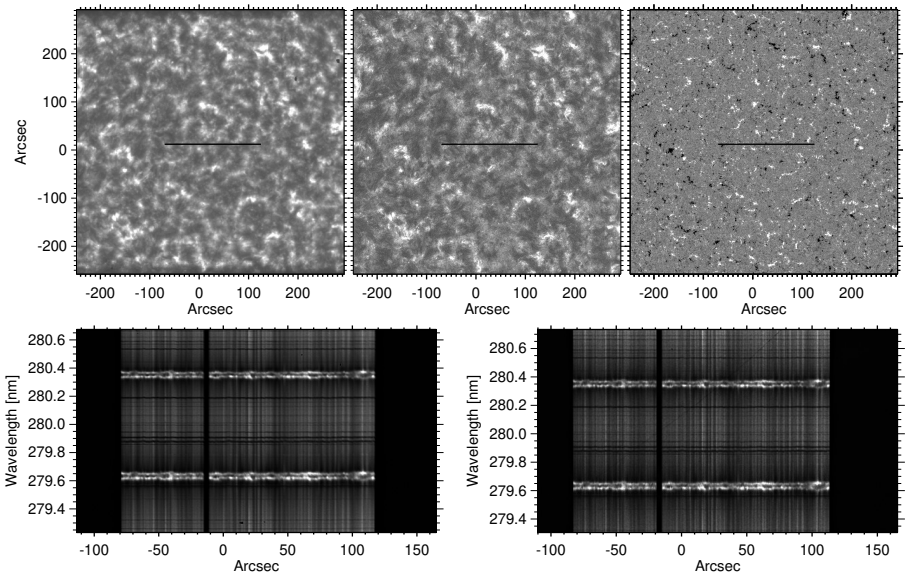

Figure 7. Top: UV images of the solar disk-center captured by the CLASP2/SJ (left) and the SDO/AIA (middle), and the photospheric magnetogram in the same field-of-view, obtained by SDO/HMI (right). The *black lines* seen in the limages represent the position of the CLASP2's spectropolarimeter slit. Bottom: the Mg II h and k spectra taken by the CLASP2 spectropolarimeter (left: channel 1 and right: channel 2). The *thick black vertical line* in the spectra is due to a dust particle located in the slit plate.

illumination field at solar disk center (Štěpán et al., 2015). In addition, the spatially averaged circular polarization due to the longitudinal Zeeman effect is zero because the quiet Sun's magnetic fields consists of mixed polarities whose signals cancel out.

Figure 7 shows the Lyα image taken by the CLASP2/SJ and co-aligned images obtained from the *Solar Dynamics Observatory* (SDO; Pesnell, Thompson, and Chamberlin, 2012). The photospheric magnetogram obtained with the SDO/*Helioseismic Magnetic Imager* (HMI; Schou et al., 2012) is aligned with the SDO/*Atmospheric Image Assembly* (AIA; Lemen et al., 2012) 30.4 nm image using the programs (aia_prep.pro and hmi_prep.pro) in the SolarSoftWare (SSW; Freeland and Handy, 1998) software package. Subsequently, both SDO images are co-aligned to the CLASP2/SJ image by cross-correlation between the SDO/AIA 30.4 nm and CLASP2/SJ images (Kubo et al., 2016).

The solid lines marked in the upper panel of Figure 7 represent the position of the CLASP2 spectropolarimeter slit on the CLASP2/SJ field-of-view (FOV). Note that CLASP2 successfully targeted the quiet region over the entire length of the slit ($\approx 198''$). Moreover, enhanced local brightening and loop-like structures implying a strong magnetic field region are not seen along the slit. In addition, the averaged strength of the longitudinal photospheric magnetic fields along the slit is verified to be small, of about 0.05 G.

The center of the CLASP2 slit is observed to be located about 30″ away from Sun center toward the northwest direction, causing a small asymmetry ($0.991 < \mu < 0.997$ over the slit). The scattering polarization is proportional to $(1 - \mu^2)$ resulting in its center-to-limb variation (CLV, Trujillo Bueno, Štěpán, and Casini, 2011). The theoretical calculation predicts **a** scattering polarization of 1.5% at the center of the Mg II k line for $\mu = 0.1$ (Belluzzi and Trujillo Bueno, 2012). Thus, the scattering polarization measured by CLASP2 during the Sun-center observations is estimated to be 0.03% at maximum ($\mu \approx 0.991$), indicating that the influence of CLV is negligibly small. Moreover, at the center of the Mg II h line, the signal is intrinsically zero (Belluzzi and Trujillo Bueno, 2012) as observationally confirmed in Rachmeler et al (2022; submitted).

The bottom panel in Figure 7 shows the Mg II spectra taken by CLASP2 at disk center. The FOV of the spectropolarimeter images fully covers our required spectral window (279.985±0.45 nm) for CLASP2, and the two brightest emission lines are the Mg II h (280.34 nm) and k (279.64 nm) lines. In these spectral images, a vertical dim region can be noticed simultaneously on both channels, which is caused by dust on the slit and is excluded from the following analysis.

6.2. Demodulated Polarization Signals and Spurious Polarization

The spurious polarization terms are determined by analyzing the in-flight data obtained from the disk center of the Sun. Figure 8 shows the demodulated Stokes I', Q'/I', U'/I', and V'/I' spectra around the Mg II h and k lines constructed by accumulating three datasets corresponding to three PMU rotations (9.6 s). Note that, we obtained four datasets corresponding to four rotations of PMU (Section 6.1), but found that the last dataset was not suitable for the polarization calibration due to abrupt intensity change. For this reason, only three datasets taken for 9.6 s were used to confirm the polarization characteristics of CLASP2. We find from the figure that the polarization signal is close to zero in most of the pixels and that the salt and pepper noise ($\approx 0.7\%$) is dominant, except for some regions in Q'/I' and U'/I' spectra. The possible source of these non-zero polarization signals is the scattering polarization induced by the local symmetry breaking (see black arrows in Figure 8).

We spatially accumulated all Stokes profiles along the slit direction (350 pixels, excluding the region affected by the dust particle), and derived the fractional polarization profile as shown in Figure 9. The averaging cancels out any possible polarization signals that may occur in the local solar structures, and also reduces the photon noise ($\approx 10^{-4}$). Note that, the spatial and temporal summation is done before dividing Q', U', and V' by I'. We find that most of the polarization signals around the Mg II line center (data points sandwitched by black solid lines in Figure 9) are distributed within or near the range of the required tolerance for the spurious polarization terms (dashed lines in Figure 9).

To determine the spurious polarization terms at the Mg II h and k lines, we performed the spectral summation of the polarization signals between the range of ±0.015 nm from each center wavelength of the Mg II h and k lines. With this summation, the photon noise is reduced to $< 10^{-4}$. Table 5 lists the demodulated Stokes q', u', and v' signals and their measurement errors, which are estimated

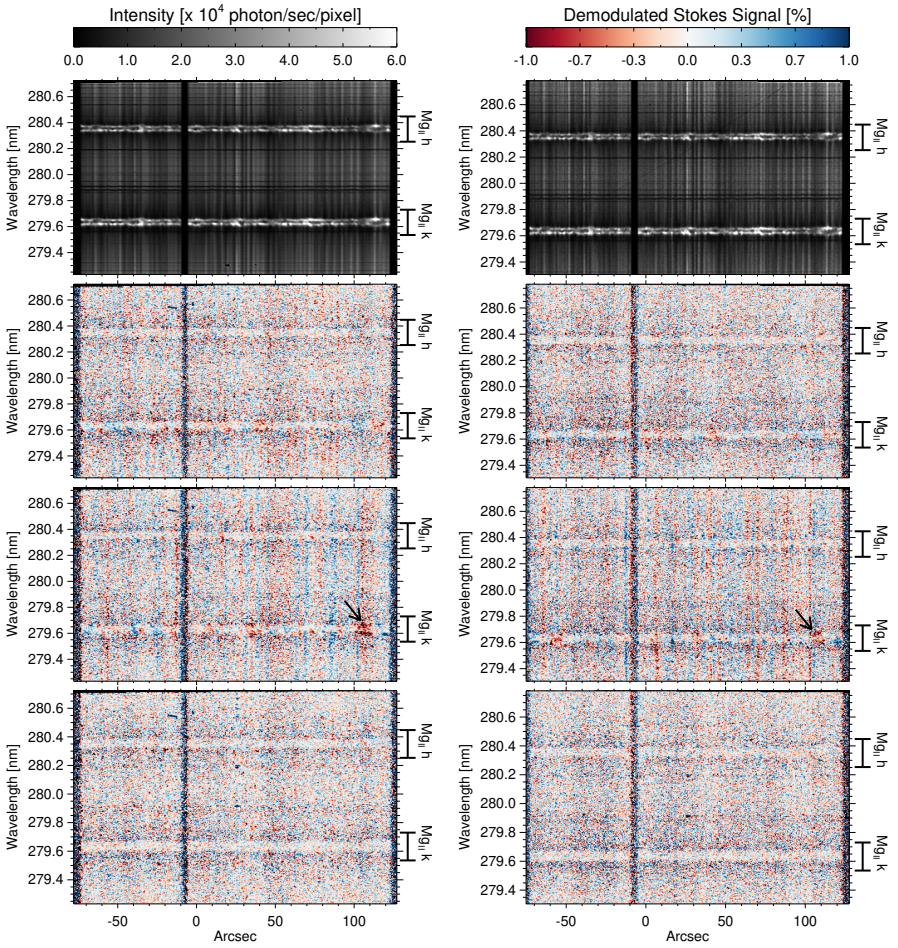

Figure 8. Stokes I', Q'/I', U'/I', and V'/I' spectra obtained near solar disk center during three PMU rotations (9.6 seconds) from channel 1 (left) and 2 (right).

Table 5. Spurious polarization at the Mg II h and k lines for both the channels. The errors are determined as $1\sigma/\sqrt{N_{pixels}}$. **All signals are expressed like the power** -4 **of** 10**.**

	Band	q' ($\times 10^{-4}$)	u' ($\times 10^{-4}$)	v' ($\times 10^{-4}$)
Channel 1	Mg II k	-1.2 ± 0.9	-0.3 ± 1.3	-0.2 ± 0.6
	Mg II h	-1.7 ± 0.8	-1.3 ± 0.9	$+1.4 \pm 0.7$
Channel 2	Mg II k	-1.1 ± 0.8	-0.2 ± 1.3	$+0.3 \pm 0.4$
	Mg II h	-0.2 ± 0.5	-0.4 ± 0.9	-0.6 ± 0.6
Channel 1+2	Mg II k	-1.1 ± 0.8	-0.3 ± 0.9	$+0.1 \pm 0.4$
	Mg II h	-1.0 ± 0.5	-0.9 ± 0.4	$+0.4 \pm 0.4$

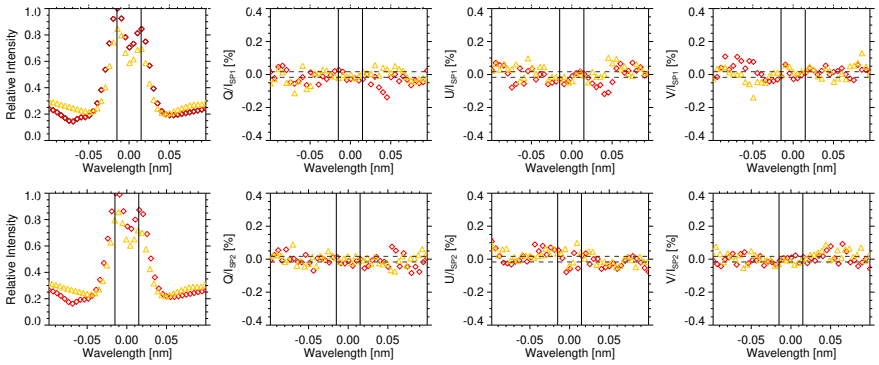

Figure 9. Spatially (350 pixels along the slit) and temporally (9.6 s; 3 PMU rotations) averaged Stokes profiles of $I', Q'/I', U'/I'$ and V'/I' obtained near the solar disk center from channel 1 (top panel) and 2 (bottom panel). The *orange* and *red colors* in the profiles represents the Mg II h and Mg II k lines, respectively.

at the Mg II h and k lines. This corresponds to the spurious polarizations of $\boldsymbol{x}_{21}$, $\boldsymbol{x}_{31}$, and $\boldsymbol{x}_{41}$. All measured polarization signals and errors at both lines are within ± 0.00017 ($\pm 1.7 \times 10^{-4}$), which satisfies our required tolerance for spurious polarization well. Here, we noted that all measured polarization signals (Table 5) were significantly smaller than the 10^{-3} level (i.e., v'), which was measured with the "un-polarized" light as tabulated in Table 4. It clearly implies that the light source used in the laboratory was not perfectly un-polarized. There is a small difference in the spurious polarizations between the Mg II h and Mg II k lines. However, this difference is smaller than their errors. Therefore, we conclude that spurious polarization does not depend on the wavelength.

6.3. Response Matrix in the Mg II h and k lines

The final response matrices of the CLASP2 at each of the Mg II h and k lines are estimated by the wavelength-dependent response matrices described in Section 5.8. That is, they were determined by substituting the central wavelengths of the Mg II h and k lines into the Equations 30 and 31. Two channels of the response matrix in the Mg II k line are

$$\boldsymbol{X}_{1,k} = \begin{pmatrix} +1.00000 & -0.01171 & -0.00631 & -0.00081 \\ -0.00012 & +0.98173 & -0.03699 & +0.00634 \\ -0.00003 & +0.03688 & +0.98196 & -0.00110 \\ -0.00002 & +0.00773 & +0.00166 & +0.99085 \end{pmatrix} \tag{32}$$

$$\boldsymbol{X}_{2,k} = \begin{pmatrix} +1.00000 & +0.00957 & -0.00587 & -0.00604 \\ -0.00011 & +0.98731 & -0.00630 & +0.00618 \\ +0.00002 & +0.00591 & +0.98812 & -0.00150 \\ -0.00003 & -0.00132 & +0.00212 & +0.99084 \end{pmatrix}, \tag{33}$$

and two channels of response matrix in the Mg II h lines are

$$\boldsymbol{X}_{1,h} = \begin{pmatrix} +1.00000 & -0.00539 & -0.00462 & +0.00019 \\ -0.00017 & +0.98854 & -0.03139 & +0.00746 \\ +0.00013 & +0.03139 & +0.98877 & -0.00131 \\ +0.00014 & +0.00686 & +0.00199 & +0.98211 \end{pmatrix}, \tag{34}$$

$$\boldsymbol{X}_{2,h} = \begin{pmatrix} +1.00000 & +0.00373 & -0.00807 & -0.00670 \\ -0.00002 & +0.99391 & -0.00041 & +0.00756 \\ +0.00004 & +0.00010 & +0.99441 & -0.00195 \\ -0.00006 & -0.00178 & +0.00214 & +0.98211 \end{pmatrix}, \tag{35}$$

where $\boldsymbol{X}_{1,k\,or\,h}$ and $\boldsymbol{X}_{2,k\,or\,h}$ represent the response matrices derived from channels 1 and channel 2, respectively. Note that, they were derived by accumulating several pixels along the spatial and wavelength directions. Here, for the spurious polarization terms of the Mg II h and k lines, the results of each line obtained from the single in-flight data were used as it is (Section 6.2).

7. Summary

We have verified the polarization characteristics of the CLASP2 instrument by determining its response matrix. The response matrix was determined by combining the polarization calibration results from pre-flight data on the ground with those from in-flight data taken from the solar disk-center observations. To this end, first, we derive the demodulated Stokes signals assuming an ideal system without wavelength dependence. Then, the response matrix was computed to compensate the difference from the assumption by accumulating several pixels along the spatial and wavelength directions to suppress the photon noise and other errors.

Our results demonstrate that the response matrices measured in the two channels of CLASP2 are close to an ideal response matrix, i.e., the scale factor and crosstalk terms of the matrix are close to 1 and 0, respectively. We confirmed the uncertainty of the response matrix element estimated by the repeatability of the results measured for eight consecutive days in the similar environment. We find that the uncertainty of a few elements for the scale factor and crosstalk verifiably has a larger value than the tolerance. However, even if such elements that are outside of the tolerance are included, the final accuracy of each Stokes parameter determined by combining all the uncertainties of the response matrix elements does meet the required tolerance. In addition, the spurious polarization terms were measured using **a** single in-flight data, and were confirmed that they are smaller than our required tolerance., This indicates that CLASP2 achieves the 0.1% polarization accuracy at 3σ level in spatially averaged data.

Finally, a non-negligible wavelength-dependent component of each response matrix element is detected over the entire CLASP2 spectral window. At the end-to-end calibration of the flight data, the demodulated polarization signals are corrected using the wavelength-dependent response matrices determined from

Table 6. Error budgets of CLASP2

Error Breakdown	Error (1σ)	
	Plage	Quiet Sun
Instrumental polarization by the CLASP2 telescope	$< 10^{-3}$ %	
Readout noise of the CCD camera	0.0009 %	0.0016 &
Photon noise of each target	0.0210 %	0.0180 %
Measurement errors in polarization calibration		
- Spurious polarization (Ishikawa et al., 2014)	< 0.0170 %	
- Scale factor	< 0.0137 %	
- Crosstalk	< 0.0137 %	
RSS (root-sum-square)	< 0.0330 %	< 0.0315 %

each channel, and then the final Stokes Q/I, U/I, and V/I signals are determined by combining the polarization signals from the two channels.

Appendix

A. Error Budgets for the CLASP2 Instrument

CLASP2 aims to achieve a polarization accuracy of 0.1% at 3σ level. The error budgets of CLASP2 are investigated to verify the performance of the instrument.

A.1. Instrumental Polarization by the CLASP2 Telescope

CLASP2 reused the classical Cassegrain telescope from the CLASP1 experiment, which has a symmetrical structure. Ishikawa et al. (2014) reported from the polarization ray tracing that the instrumental polarization caused by off-axis incidence at $\pm 200''$ in CLASP1 was negligibly small. Based on this result, we assume that the influence of the off-axis incidence for CLASP2 is negligible, because the CLASP2 FOV is half that of CLASP1.

Meanwhile, for CLASP2, we re-coated the primary mirror with **a** dual-band pass "cold-mirror" coating (Yoshida et al., 2018). This allowed us to successfully achieve high reflectivity not only in the spectral window of Mg II h and k lines (280 nm), but also in the Lyα line (121.6 nm) for the SJ. However, the non-uniformity of this new coating can cause instrumental polarization. To evaluate the coating performance, we measured the reflectivity with p- and $s-$polarized beams around 280 nm of ten witness samples (1-inch flat mirrors), which are evenly deployed over the effective area of the primary mirror and coated simultaneously with the primary mirror (Song et al., 2017a).

The reflectivity of the witness samples is verified to be uniform over the ten witness samples within $\pm 2\%$. In addition, the reflectivity between the p- and s-polarized Mg II beams are confirmed to be the same within 0.1 %. Ishikawa et al. (2014) evaluated that the coating non-uniformity within $\pm 2\%$ can suppress the

instrumental polarization down to 10^{-3}%, which is negligibly small compared to other terms in Table 6.

A.2. Spurious Polarization by Photon Noise of CLASP2 Targets

The photon noise can limit the polarization sensitivity of CLASP2. Therefore, it is important to estimate the photon noise for each scientific targets of CLASP2: plage and quiet Sun near the limb. To this end, we measured the typical Mg II intensity in a plage (1.0×10^{17} [photon cm^{-2} sec^{-1} sr^{-1} Å^{-1}]) and a quiet Sun (2.0×10^{16} [photon cm^{-2} sec^{-1} sr^{-1} Å^{-1}]) by using the Mg II spectral data obtained from IRIS (De Pontieu et al., 2014b). Moreover, the number of photons are estimated by using the parameters of CLASP2 (spatial plate scale: 0.″55 /pixel, spectral plate scale: 0.005 nm/pixel, slit width: 0.″55, and photon throughput for all the optical components: 1.8%) as well as the scientific requirements for each target of a plage, i.e., 0.01 nm spectral resolution (2 pixels), $2'' - 3''$ spatial-resolution (4 pixels), and 2.5-minute observations (754 exposures) and a quiet Sun, i.e., 0.02 nm spectral resolution (4 pixels), $10'' - 11''$ spatial resolutions (20 pixels), and 2.3-minutes observation (690 exposures)). Subsequently, the expected total number of photons (N_{tot}) are 8.5×10^7 (plage) and 1.5×10^8 (quiet Sun).

The spurious polarization caused by the photon noise is evaluated by

$$\Delta S'_{PN} = \frac{1}{a_1 \sqrt{N_{tot}}}, \tag{36}$$

where, $a_1 = 0.505$ that is a modulation coefficient when the phase retardation of the CLASP2 waveplate is 234° (see, Section 3.2). Therefore, the anticipated spurious polarizations by the photon noise are 0.021% at the plage and 0.018% at the quiet Sun near the limb.

A.3. Spurious Polarization Caused by the Readout Noise of the CLASP2 Spectropolarimeter Camera

The readout noise (σ) of the CLASP2 spectropolarimeter camera is about 5.1 photon/exposure from one exposure. Based on the measured readout noise of the spectropolarimeter camera, the estimated spurious polarization caused by the readout noise is

$$\Delta S'_{RN} = \frac{\sqrt{n \times s_\lambda \times s_d}\sigma}{a_1 N_{tot}} \tag{37}$$

where, N_{tot} and a_1 are identical to the parameters explained in Appendix A.2. n and s are the total number of exposure and the number of pixels summed along the slit, respectively ($n = 754$ exposures and $s_\lambda = 2$ pixels and $s_d = 4$ pixels at the plage and $n = 690$ exposures and $s_\lambda = 4$ pixels and $s_d = 20$ pixels at the quiet Sun). The measured spurious polarizations with these parameters are 0.0005% (plage) and 0.0007% (quiet Sun).

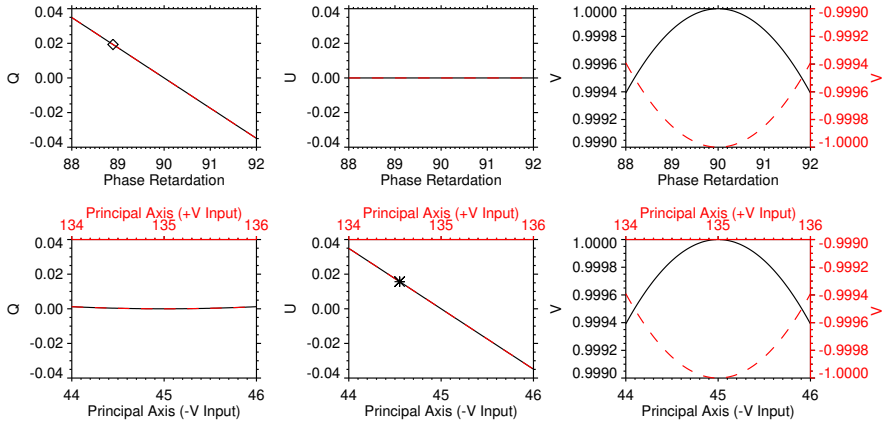

Figure 10. Variations of Stokes parameters Q, U, and V of the light source depending on the phase retardations (top) and the angles of the principal axis (bottom) of a quarter-waveplate installed inside the light source chamber. The *black lines* are for the configuration of $-V$ input (the nominal angle of the principal axis of the quarter waveplate χ is 45°), and the *red dashed lines* are for the configuration of $+V$ input ($\chi = 135°$). The *black diamond* and the *asterisk* represent the average signals of the residual Stokes Q and U parameters measured from $\pm V$ inputs.

B. Imperfection of the Light Source System

B.1. Measurement Accuracy of the Phase Retardation for the Linear Polarizer and Misalignment between the Waveplate and the Linear Polarizer

The demodulated polarization signals of q' and u' should show opposite signs between $+V$ and $-V$ inputs (Equation 17). However, as discussed in Section 5.3, $V \rightarrow Q$ and U crosstalks have the same sign and are greater than 0.01 (maximum signal is about 0.029 at $+V$ input of both channels) on both channels.

Next, we investigate whether this behavior can be explained by the imperfection of the light source that is used for the polarization calibration. Note that the phase retardation of the quarter waveplate $\delta_{1/4}$ of the light source may not be exactly 90° and the misalignment of the principal axis for the quarter waveplate installed inside the light source chamber may exist. The output beam from the light source system can be expressed as $[I, Q, U, V]^\top = [1, \cos 2^2\chi + \sin 2^2\chi \cos\delta_{1/4}, \cos 2\chi \sin 2\chi(1 - \cos\delta_{1/4}), \sin 2\chi \sin\delta_{1/4}]^\top$ in the Stokes vector form. Here, χ is the angle of the principal axis for the quarter waveplate with respect to the X-axis of the CLASP2 coordinate system. In the ideal case, $\chi = 135°$ and $\chi = 45°$ for $+V$ and $-V$ inputs, respectively. Note that the principal axis of the polarizer is set to the X-axis of the CLASP2 coordinate system and the linear polarization imparted to the quarter waveplate is $[1, 1, 0, 0]^\top$.

Figure 10 shows the polarization states of the light source as a function of $\delta_{1/4}$ and χ. This figure clearly shows that the residual Q and U can be caused by $\delta_{1/4} \neq 90°$ and $\chi \neq 135°$ or $\chi \neq 45°$, respectively. The residual Q signal can be

explained by $\delta_{1/4} \approx 89°$ (a diamond symbol in Figure 10). The phase retardation is wavelength-dependent and such a deviation by 1° is possible considering the measurement accuracy of the phase retardation. Similarly, the misalignment of the principal axis for the quarter waveplate by $\approx 0.5°$ is possible, which is comparable to the worst-case accuracy of the angle of the principal axis of the waveplate. On the other hand, the change in the V signal caused by such imperfection of the light source is small enough to be negligible as $\approx 10^{-4}$.

Based on these findings, the change of the response matrices due to the imperfection of the light source for circularly polarized input is investigated. We find from Figure 10 that the degree of polarization of the V input is approximately 0.9998 when $\delta_{1/4} \neq 90°$, $\chi \neq 135°$, or $\chi \neq 45°$. This uncertainty of V input beam mainly affects the accuracy of the scale factor of $\boldsymbol{x}_{44}$ and the crosstalks of $\boldsymbol{x}_{14}$, $\boldsymbol{x}_{24}$, and $\boldsymbol{x}_{34}$. Assuming that the degree of polarization of the V input beam is 0.9998, the representative response matrices (Equations 26 and 27) can be rewritten as follow:

$$\boldsymbol{X}_1 = \begin{pmatrix} 1 & -0.00846 & -0.00550 & -0.00025 \\ 0 & +0.98549 & -0.03445 & +0.00682 \\ 0 & +0.03418 & +0.98621 & -0.00111 \\ 0 & +0.00743 & +0.00186 & +\mathbf{0.98667} \end{pmatrix} \begin{pmatrix} \\ \\ \\ \\ \end{pmatrix} \tag{38}$$

$$\boldsymbol{X}_2 = \begin{pmatrix} 1 & +0.00692 & -0.00704 & -0.00636 \\ 0 & +0.99088 & -0.00350 & +0.00693 \\ 0 & +0.00314 & +0.99119 & -0.00168 \\ 0 & -0.00143 & +0.00219 & +\mathbf{0.98675} \end{pmatrix} \begin{pmatrix} \\ \\ \\ \\ \end{pmatrix}. \tag{39}$$

We find that $\boldsymbol{x}_{44}$ (bold text) of the renewed response matrices increases by ≈ 0.0002, but other elements remain the same as before. If we assume that the maximum degree of polarization in the solar observations is 3%, the change of $\boldsymbol{x}_{44}$ results in the scale error of 0.0006%, which is negligible since the error is sufficiently small.

B.2. Contamination of the v Signal in $\pm Q$ and $\pm U$ Inputs

We raise the possibility that the linear polarization beam from the light source was not completely linearly polarized, and we estimated the contamination of the circular polarization signal (Δv) for the input beam under such an assumption. If v is not zero ($v \neq 0$), the demodulated polarization signals of v' (see, Equation 14) for $\pm Q$ and $\pm U$ inputs are given by

$$[v']_{\pm Q} = \frac{x_{41} + q x_{42} + u x_{43} + v x_{44}}{1 + q x_{12} + u x_{13} + v x_{14}} \sim \frac{\pm x_{42} + \Delta v}{1 \pm x_{12}} \tag{40}$$

with $(1,q,u,v)^\top = (1,\pm 1,0,v \neq 0)^\top$ and

$$[v']_{\pm U} = \frac{x_{41} + q x_{42} + u x_{43} + v x_{44}}{1 + q x_{12} + u x_{13} + v x_{14}} \sim \frac{\pm x_{43} + \Delta v}{1 \pm x_{13}} \tag{41}$$

with $(1,\mathrm{q},\mathrm{u},\mathrm{v})^\top=(1,0,\pm1,\mathrm{v}\neq0)^\top$. Subsequently, the contaminated v signals are estimated by

$$\Delta v = \frac{1}{2}([v']_{+Q}(1+\boldsymbol{x}_{12}) - [v']_{-Q}(1-\boldsymbol{x}_{12})) \tag{42}$$

and

$$\Delta v = \frac{1}{2}([v']_{+U}(1+\boldsymbol{x}_{13}) - [v']_{-U}(1-\boldsymbol{x}_{13})). \tag{43}$$

The average v-contamination measured from Equations 42 and 43 is about 0.0035 on both the channels. Therefore, it is confirmed that v-contamination may exist in the linear polarization beam emitted from the light source. However, the influence of v-contamination can be neglected when determining each element of the response matrix. This is because the v-contamination is compeletely cancelled out while solving the respective simultaneous equations shown in $[v']_{\pm Q}$ and $[v']_{\pm U}$ to estimate the elements of $\boldsymbol{x}_{42}$ and $\boldsymbol{x}_{43}$ (Equations 40 and 41).

B.3. Polarization Degree of the Light Source

The polarization degree of our light source used in the pre-flight calibration is determined by the extinction ratio (r_e) of the linear polarizer installed inside the light source chamber. Before the integration of the light source, in 2018, we measured an extinction ratio of 400, leading to the polarization degree of the light source as $p = \frac{r_e-1}{r_e+1} \approx 0.995$. However, the extinction ratio was measured to be $r_e > 2000$ (corresponding to $p \approx 0.999$) by the vendor in 2013. There are two possibilities for this difference. The first is the aging of the linear polarizer, and second is caused by our experimental environment. The measurement of r_e can be significantly influenced by the scattered light in a laboratory, which leads to underestimation of r_e.

Next, we investigated the change of the response matrix depending on the polarization degree of the light source. Assuming that the polarization degree of the input beam is 0.995, the representative response matrices, as shown in Equations 26 and 27, are changed as follows:

$$\boldsymbol{X}_1 = \begin{pmatrix} 1 & -0.00850 & -0.00553 & -0.00026 \\ 0 & \mathbf{+0.99044} & -0.03445 & +0.00682 \\ 0 & +0.03418 & \mathbf{+0.99112} & -0.00111 \\ 0 & +0.00743 & +0.00186 & \mathbf{+0.99175} \end{pmatrix} \begin{pmatrix} \\ \\ \\ \\ \end{pmatrix} \tag{44}$$

$$\boldsymbol{X}_2 = \begin{pmatrix} 1 & +0.00696 & -0.00705 & -0.00636 \\ 0 & \mathbf{+0.99586} & -0.00350 & +0.00693 \\ 0 & +0.00314 & \mathbf{+0.99617} & -0.00168 \\ 0 & -0.00143 & +0.00219 & \mathbf{+0.99291} \end{pmatrix} \begin{pmatrix} \\ \\ \\ \\ \end{pmatrix}. \tag{45}$$

From Equations 44 and 45, the values of the diagonal (bold text) of the renewed response matrices increases by ≈ 0.005 to close to unity, but other elements of the crosstalk remain the same as before. The change of the diagonal component results in the scale error of 0.015 % if the degree of the polarization

is 3%, which is the maximum value expected for the solar observations (see Section 3.4). This error is sufficiently small that using the vendor supplied r_e is sufficient and any reduction of r_e is neglected from degradation or experimental environment.

Acknowledgments CLASP2 is an international partnership between NASA/MSFC, NAOJ, JAXA, IAC, and IAS; additional partners include ASCR, IRSOL, LMSAL, and the University of Oslo. The Japanese participation was funded by ISAS/JAXA as a Small Mission-of-Opportunity Program, JSPS KAKENHI Grant numbers JP25220703 and JP16H03963, 2015 ISAS Grant for Promoting International Mission Collaboration, and by 2016 NAOJ Grant for Development Collaboration. The USA participation was funded by NASA Award 16-HTIDS16_2-0027. The Spanish participation was funded by the European Research Council (ERC) under the European Union's Horizon 2020 research and innovation programme (Advanced Grant agreement No. 742265). The French hardware participation was funded by CNES funds CLASP2-13616A and 13617A. IRSOL participation was founded by SNSF through grants 200021_175997 and CRSII5_180238

References

Alsina Ballester, E., Belluzzi, L., Trujillo Bueno, J.: 2016, The Magnetic Sensitivity of the Mg II k Line to the Joint Action of Hanle, Zeeman, and Magneto-optical Effects. *Astrophys. J. Lett.* **831**, L15. DOI. ADS.

Belluzzi, L., Trujillo Bueno, J.: 2012, The Polarization of the Solar Mg II h and k Lines. *Astrophys. J. Lett.* **750**, L11. DOI. ADS.

Berger, T., Mudge, J., Holmes, B., Searcy, P., Wuelser, J.P., Lemen, J., Title, A.: 2012, Design and fabrication of the near-ultraviolet birefringent Solc filter for the NASA IRIS solar physics mission. In: Johnson, R.B., Mahajan, V.N., Thibault, S. (eds.) *Current Developments in Lens Design and Optical Engineering XIII*, *SPIE Conf. Ser.* **8486**, 84860G. DOI. ADS.

De Pontieu, B., Rouppe van der Voort, L., McIntosh, S.W., Pereira, T.M.D., Carlsson, M., Hansteen, V., Skogsrud, H., Lemen, J., Title, A., Boerner, P., Hurlburt, N., Tarbell, T.D., Wuelser, J.P., De Luca, E.E., Golub, L., McKillop, S., Reeves, K., Saar, S., Testa, P., Tian, H., Kankelborg, C., Jaeggli, S., Kleint, L., Martinez-Sykora, J.: 2014a, On the prevalence of small-scale twist in the solar chromosphere and transition region. *Science* **346**, 1255732. DOI. ADS.

De Pontieu, B., Title, A.M., Lemen, J.R., Kushner, G.D., Akin, D.J., Allard, B., Berger, T., Boerner, P., Cheung, M., Chou, C., Drake, J.F., Duncan, D.W., Freeland, S., Heyman, G.F., Hoffman, C., Hurlburt, N.E., Lindgren, R.W., Mathur, D., Rehse, R., Sabolish, D., Seguin, R., Schrijver, C.J., Tarbell, T.D., Wülser, J.-P., Wolfson, C.J., Yanari, C., Mudge, J., Nguyen-Phuc, N., Timmons, R., van Bezooijen, R., Weingrod, I., Brookner, R., Butcher, G., Dougherty, B., Eder, J., Knagenhjelm, V., Larsen, S., Mansir, D., Phan, L., Boyle, P., Cheimets, P.N., DeLuca, E.E., Golub, L., Gates, R., Hertz, E., McKillop, S., Park, S., Perry, T., Podgorski, W.A., Reeves, K., Saar, S., Testa, P., Tian, H., Weber, M., Dunn, C., Eccles, S., Jaeggli, S.A., Kankelborg, C.C., Mashburn, K., Pust, N., Springer, L., Carvalho, R., Kleint, L., Marmie, J., Mazmanian, E., Pereira, T.M.D., Sawyer, S., Strong, J., Worden, S.P., Carlsson, M., Hansteen, V.H., Leenaarts, J., Wiesmann, M., Aloise, J., Chu, K.-C., Bush, R.I., Scherrer, P.H., Brekke, P., Martinez-Sykora, J., Lites, B.W., McIntosh, S.W., Uitenbroek, H., Okamoto, T.J., Gummin, M.A., Auker, G., Jerram, P., Pool, P., Waltham, N.: 2014b, The Interface Region Imaging Spectrograph (IRIS). *Solar Phys.* **289**, 2733. DOI. ADS.

De Pontieu, B., Polito, V., Hansteen, V., Testa, P., Reeves, K.K., Antolin, P., Nóbrega-Siverio, D.E., Kowalski, A.F., Martinez-Sykora, J., Carlsson, M., McIntosh, S.W., Liu, W., Daw, A., Kankelborg, C.C.: 2021, A New View of the Solar Interface Region from the Interface Region Imaging Spectrograph (IRIS). *Solar Phys.* **296**, 84. DOI. ADS.

del Pino Alemán, T., Casini, R., Manso Sainz, R.: 2016, Magnetic Diagnostics of the Solar Chromosphere with the Mg II h-k Lines. *Astrophys. J. Lett.* **830**, L24. DOI. ADS.

del Pino Alemán, T., Trujillo Bueno, J., Casini, R., Manso Sainz, R.: 2020, The Magnetic Sensitivity of the Resonance and Subordinate Lines of Mg II in the Solar Chromosphere. *Astrophys. J.* **891**, 91. DOI. ADS.

Elmore, D.F.: 1990, *A polarization calibration technique for the Advanced Stokes Polarimeter*, NCAR Technical Note, NCAR/TN-355+STR, Boulder, Colorado.

Freeland, S.L., Handy, B.N.: 1998, Data Analysis with the SolarSoft System. *Solar Phys.* **182**, 497. DOI. ADS.

Giono, G., Ishikawa, R., Narukage, N., Kano, R., Katsukawa, Y., Kubo, M., Ishikawa, S., Bando, T., Hara, H., Suematsu, Y., Winebarger, A., Kobayashi, K., Auchère, F., Trujillo Bueno, J.: 2016, Polarization Calibration of the Chromospheric Lyman-Alpha SpectroPolarimeter for a 0.1 % Polarization Sensitivity in the VUV Range. Part I: Pre-flight Calibration. *Solar Phys.* **291**, 3831. DOI. ADS.

Giono, G., Ishikawa, R., Narukage, N., Kano, R., Katsukawa, Y., Kubo, M., Ishikawa, S., Bando, T., Hara, H., Suematsu, Y., Winebarger, A., Kobayashi, K., Auchère, F., Trujillo Bueno, J., Tsuneta, S., Shimizu, T., Sakao, T., Cirtain, J., Champey, P., Asensio Ramos, A., Štěpán, J., Belluzzi, L., Manso Sainz, R., De Pontieu, B., Ichimoto, K., Carlsson, M., Casini, R., Goto, M.: 2017, Polarization Calibration of the Chromospheric Lyman-Alpha SpectroPolarimeter for a 0.1% Polarization Sensitivity in the VUV Range. Part II: In-Flight Calibration. *Solar Phys.* **292**, 57. DOI. ADS.

Ichimoto, K., Lites, B., Elmore, D., Suematsu, Y., Tsuneta, S., Katsukawa, Y., Shimizu, T., Shine, R., Tarbell, T., Title, A., Kiyohara, J., Shinoda, K., Card, G., Lecinski, A., Streander, K., Nakagiri, M., Miyashita, M., Noguchi, M., Hoffmann, C., Cruz, T.: 2008, Polarization Calibration of the Solar Optical Telescope onboard Hinode. *Solar Phys.* **249**, 233. DOI. ADS.

Ishikawa, R., Kano, R., Bando, T., Suematsu, Y., Ishikawa, S.-n., Kubo, M., Narukage, N., Hara, H., Tsuneta, S., Watanabe, H., Ichimoto, K., Aoki, K., Miyagawa, K.: 2013, Birefringence of magnesium fluoride in the vacuum ultraviolet and application to a half-waveplate. *Appl. Opt.* **52**, 8205. DOI. ADS.

Ishikawa, R., Narukage, N., Kubo, M., Ishikawa, S., Kano, R., Tsuneta, S.: 2014, Strategy for Realizing High-Precision VUV Spectro-Polarimeter. *Solar Phys.* **289**, 4727. DOI. ADS.

Ishikawa, R., Trujillo Bueno, J., Uitenbroek, H., Kubo, M., Tsuneta, S., Goto, M., Kano, R., Narukage, N., Bando, T., Katsukawa, Y., Ishikawa, S., Giono, G., Suematsu, Y., Hara, H., Shimizu, T., Sakao, T., Winebarger, A., Kobayashi, K., Cirtain, J., Champey, P., Auchère, F., Štěpán, J., Belluzzi, L., Asensio Ramos, A., Manso Sainz, R., De Pontieu, B., Ichimoto, K., Carlsson, M., Casini, R.: 2017, Indication of the Hanle Effect by Comparing the Scattering Polarization Observed by CLASP in the Lyα and Si III 120.65 nm Lines. *Astrophys. J.* **841**, 31. DOI. ADS.

Ishikawa, R., Bueno, J.T., del Pino Alemán, T., Okamoto, T.J., McKenzie, D.E., Auchère, F., Kano, R., Song, D., Yoshida, M., Rachmeler, L.A., Kobayashi, K., Hara, H., Kubo, M., Narukage, N., Sakao, T., Shimizu, T., Suematsu, Y., Bethge, C., De Pontieu, B., Dalda, A.S., Vigil, G.D., Winebarger, A., Ballester, E.A., Belluzzi, L., Štěpán, J., Ramos, A.A., Carlsson, M., Leenaarts, J.: 2021, Mapping solar magnetic fields from the photosphere to the base of the corona. *Scien. Adv.* **7**, eabe8406. DOI. ADS.

Ishikawa, S., Shimizu, T., Kano, R., Bando, T., Ishikawa, R., Giono, G., Tsuneta, S., Nakayama, S., Tajima, T.: 2015, Development of a Precise Polarization Modulator for UV Spectropolarimetry. *Solar Phys.* **290**, 3081. DOI. ADS.

Kano, R., Bando, T., Narukage, N., Ishikawa, R., Tsuneta, S., Katsukawa, Y., Kubo, M., Ishikawa, S.-n., Hara, H., Shimizu, T., Suematsu, Y., Ichimoto, K., Sakao, T., Goto, M., Kato, Y., Imada, S., Kobayashi, K., Holloway, T., Winebarger, A., Cirtain, J., De Pontieu, B., Casini, R., Trujillo Bueno, J., Štepán, J., Manso Sainz, R., Belluzzi, L., Asensio Ramos, A., Auchère, F., Carlsson, M.: 2012, Chromospheric Lyman-alpha spectro-polarimeter (CLASP). In: Takahashi, T., Murray, S.S., den Herder, J.-W.A. (eds.) *Space Telescopes and Instrumentation 2012: Ultraviolet to Gamma Ray*, *SPIE Conf. Ser.* **8443**, 84434F. DOI. ADS.

Kano, R., Trujillo Bueno, J., Winebarger, A., Auchère, F., Narukage, N., Ishikawa, R., Kobayashi, K., Bando, T., Katsukawa, Y., Kubo, M., Ishikawa, S., Giono, G., Hara, H., Suematsu, Y., Shimizu, T., Sakao, T., Tsuneta, S., Ichimoto, K., Goto, M., Belluzzi, L., Štěpán, J., Asensio Ramos, A., Manso Sainz, R., Champey, P., Cirtain, J., De Pontieu, B.,

Casini, R., Carlsson, M.: 2017, Discovery of Scattering Polarization in the Hydrogen Lyα Line of the Solar Disk Radiation. *Astrophys. J. Lett.* **839**, L10. DOI. ADS.

Kubo, M., Katsukawa, Y., Suematsu, Y., Kano, R., Bando, T., Narukage, N., Ishikawa, R., Hara, H., Giono, G., Tsuneta, S., Ishikawa, S., Shimizu, T., Sakao, T., Winebarger, A., Kobayashi, K., Cirtain, J., Champey, P., Auchère, F., Trujillo Bueno, J., Asensio Ramos, A., Štěpán, J., Belluzzi, L., Manso Sainz, R., De Pontieu, B., Ichimoto, K., Carlsson, M., Casini, R., Goto, M.: 2016, Discovery of Ubiquitous Fast-Propagating Intensity Disturbances by the Chromospheric Lyman Alpha Spectropolarimeter (CLASP). *Astrophys. J.* **832**, 141. DOI. ADS.

Lemen, J.R., Title, A.M., Akin, D.J., Boerner, P.F., Chou, C., Drake, J.F., Duncan, D.W., Edwards, C.G., Friedlaender, F.M., Heyman, G.F., Hurlburt, N.E., Katz, N.L., Kushner, G.D., Levay, M., Lindgren, R.W., Mathur, D.P., McFeaters, E.L., Mitchell, S., Rehse, R.A., Schrijver, C.J., Springer, L.A., Stern, R.A., Tarbell, T.D., Wuelser, J.-P., Wolfson, C.J., Yanari, C., Bookbinder, J.A., Cheimets, P.N., Caldwell, D., Deluca, E.E., Gates, R., Golub, L., Park, S., Podgorski, W.A., Bush, R.I., Scherrer, P.H., Gummin, M.A., Smith, P., Auker, G., Jerram, P., Pool, P., Soufli, R., Windt, D.L., Beardsley, S., Clapp, M., Lang, J., Waltham, N.: 2012, The Atmospheric Imaging Assembly (AIA) on the Solar Dynamics Observatory (SDO). *Solar Phys.* **275**, 17. DOI. ADS.

Narukage, N., Auchère, F., Ishikawa, R., Kano, R., Tsuneta, S., Winebarger, A.R., Kobayashi, K.: 2015, Vacuum ultraviolet spectropolarimeter design for precise polarization measurements. *Appl. Opt.* **54**, 2080. DOI. ADS.

Narukage, N., McKenzie, D.E., Ishikawa, R., Trujillo-Bueno, J., De Pontieu, B., Kubo, M., Ishikawa, S.-n., Kano, R., Suematsu, Y., Yoshida, M., Rachmeler, L.A., Kobayashi, K., Cirtain, J.W., Winebarger, A.R., Asensio Ramos, A., del Pino Aleman, T., Štěpán, J., Belluzzi, L., Larruquert, J.I., Auchère, F., Leenaarts, J., Carlsson, M.J.L.: 2016, Chromospheric LAyer SpectroPolarimeter (CLASP2). In: den Herder, J.-W.A., Takahashi, T., Bautz, M. (eds.) *Space Telescopes and Instrumentation 2016: Ultraviolet to Gamma Ray*, *SPIE Conf. Ser.* **9905**, 990508. DOI. ADS.

Okamoto, T.J., Antolin, P., De Pontieu, B., Uitenbroek, H., Van Doorsselaere, T., Yokoyama, T.: 2015, Resonant Absorption of Transverse Oscillations and Associated Heating in a Solar Prominence. I. Observational Aspects. *Astrophys. J.* **809**, 71. DOI. ADS.

Pesnell, W.D., Thompson, B.J., Chamberlin, P.C.: 2012, The Solar Dynamics Observatory (SDO). *Solar Phys.* **275**, 3. DOI. ADS.

Ruyten, W.: 1999, Smear Correction for Frame Transfer Charge-coupled-device Cameras. *Opt.Lett.* **24**, 878.

Schou, J., Scherrer, P.H., Bush, R.I., Wachter, R., Couvidat, S., Rabello-Soares, M.C., Bogart, R.S., Hoeksema, J.T., Liu, Y., Duvall, T.L., Akin, D.J., Allard, B.A., Miles, J.W., Rairden, R., Shine, R.A., Tarbell, T.D., Title, A.M., Wolfson, C.J., Elmore, D.F., Norton, A.A., Tomczyk, S.: 2012, Design and Ground Calibration of the Helioseismic and Magnetic Imager (HMI) Instrument on the Solar Dynamics Observatory (SDO). *Solar Phys.* **275**, 229. DOI. ADS.

Shimizu, T., Watanabe, K., Nakayama, S., Tajima, T., Obara, S., Imada, S., Nishizuka, N., Ishikawa, S.-n., Hara, H.: 2014, New developments in rotating and linear motion mechanisms used in contamination sensitive space telescopes. In: Navarro, R., Cunningham, C.R., Barto, A.A. (eds.) *Advances in Optical and Mechanical Technologies for Telescopes and Instrumentation*, *SPIE Conf. Ser.* **9151**, 915138. DOI. ADS.

Song, D., Ishikawa, R., Kano, R., Shinoda, K., Yoshida: 2017a, Performance Verification of the VUV Coating for the CLASP2 Flight Mirrors. In: *Accelerators and Instruments*, *UVSOR Activity Report* **45**, 36.

Song, D., Chae, J., Kwak, H., Kano, R., Yurchyshyn, V., Moon, Y.-J., Lim, E.-K., Lee, J.: 2017b, Three-minute Sunspot Oscillations Driven by Magnetic Reconnection in a Light Bridge. *Astrophys. J. Lett.* **850**, L33. DOI. ADS.

Song, D., Ishikawa, R., Kano, R., Yoshida, M., Tsuzuki, T., Uraguchi, F., Shinoda, K., Hara, H., Okamoto, T.J., Auchère, F., McKenzie, D.E., Rachmeler, L.A., Trujillo Bueno, J.: 2018, Optical alignment of the high-precision UV spectro-polarimeter (CLASP2). In: den Herder, J.-W.A., Nikzad, S., Nakazawa, K. (eds.) *Space Telescopes and Instrumentation 2018: Ultraviolet to Gamma Ray*, *SPIE Conf. Ser.* **10699**, 106992W. DOI. ADS.

Tian, H., DeLuca, E., Reeves, K.K., McKillop, S., De Pontieu, B., Martínez-Sykora, J., Carlsson, M., Hansteen, V., Kleint, L., Cheung, M., Golub, L., Saar, S., Testa, P., Weber, M., Lemen, J., Title, A., Boerner, P., Hurlburt, N., Tarbell, T.D., Wuelser, J.P., Kankelborg, C., Jaeggli, S., McIntosh, S.W.: 2014, High-resolution Observations of the Shock Wave Behavior

for Sunspot Oscillations with the Interface Region Imaging Spectrograph. *Astrophys. J.* **786**, 137. DOI. ADS.

Trujillo Bueno, J., Štěpán, J., Casini, R.: 2011, The Hanle Effect of the Hydrogen Lyα Line for Probing the Magnetism of the Solar Transition Region. *Astrophys. J. Lett.* **738**, L11. DOI. ADS.

Tsuzuki, T., Ishikawa, R., Kano, R., Narukage, N., Song, D., Yoshida, M., Uraguchi, F., Okamoto, T.J., McKenzie, D., Kobayashi, K., Rachmeler, L., Auchere, F., Trujillo Bueno, J.: 2020, Optical design of the Chromospheric LAyer Spectro-Polarimeter (CLASP2). In: *Space Telescopes and Instrumentation 2020: Ultraviolet to Gamma Ray*, *SPIE Conf. Ser.* **11444**, 114446W. DOI. ADS.

Štěpán, J., Trujillo Bueno, J., Leenaarts, J., Carlsson, M.: 2015, Three-dimensional Radiative Transfer Simulations of the Scattering Polarization of the Hydrogen Lyα Line in a Magnetohydrodynamic Model of the Chromosphere-Corona Transition Region. *Astrophys. J.* **803**, 65. DOI. ADS.

Yoshida, M., Song, D., Ishikawa, R., Kano, R., Katsukawa, Y., Suematsu, Y., Narukage, N., Kubo, M., Shinoda, K., Okamoto, T.J., McKenzie, D.E., Rachmeler, L.A., Auchère, F., Trujillo Bueno, J.: 2018, Wavefront error measurements and alignment of CLASP2 telescope with a dual-band pass cold mirror coated primary mirror. In: den Herder, J.-W.A., Nikzad, S., Nakazawa, K. (eds.) *Space Telescopes and Instrumentation 2018: Ultraviolet to Gamma Ray*, *SPIE Conf. Ser.* **10699**, 1069930. DOI. ADS.